Expanded FLP toolbox for spatiotemporal protein degradation and transcriptomic profiling in *C. elegans*

Adrián Fragoso-Luna[1,4], Raquel Romero-Bueno[1,4], Michael Eibl[1,4], Cristina Ayuso[1], Celia Muñoz-Jiménez[1], Vladimir Benes[2], Ildefonso Cases[1], Peter Askjaer[3]

[1] Andalusian Centre for Developmental Biology, Consejo Superior de Investigaciones Científicas (CSIC), Universidad Pablo de Olavide, Junta de Andalucía, Carretera de Utrera, km 1, 41013 Sevilla, Spain

[2] EMBL GeneCore, Meyerhofstrasse 1, 69117 Heidelberg, Germany

[3] Corresponding author (pask@upo.es)

[4] These authors contributed equally

Keywords: DamID; FLP/FRT recombination; GFPdeg; RAPID; spatiotemporal gene expression control; targeted protein degradation

Abstract

Control of gene expression in specific tissues and/or at certain stages of development allows the study and manipulation of gene function with high precision. Site-specific genome recombination by the Flippase (FLP) and Cre enzymes has proven particularly relevant. Joint efforts of many research groups have led to the creation of efficient FLP and Cre drivers to regulate gene expression in a variety of tissues in *Caenorhabditis elegans*. Here, we extend this toolkit by the addition of FLP lines that drive recombination specifically in distal tip cells, the somatic gonad, coelomocytes and the epithelial P lineage. In some cases, recombination-mediated gene knockouts do not completely deplete protein levels due to persistence of long-lived proteins. To overcome this, we developed a spatiotemporally regulated degradation system for GFP fusion proteins (GFPdeg) based on FLP-mediated recombination. Using two stable nuclear pore proteins, MEL-28/ELYS and NPP-2/NUP85 as examples, we report the benefit of combining tissue-specific gene knockout and protein degradation to achieve complete protein depletion. We also demonstrate that FLP-mediated recombination can be utilized to identify transcriptomes in a *C. elegans* tissue of interest. We have adapted RNA polymerase DamID (RAPID) for the FLP toolbox and by focusing on a well-characterized tissue, the hypodermis, we show that the vast majority of genes identified by RAPID are known to be expressed in this tissue. These tools allow combining FLP activity for simultaneous gene inactivation and transcriptomic profiling, thus enabling the inquiry of gene function in various complex biological processes.

Introduction

The nematode *C. elegans* is a popular model organism for genetic and biomedical research. A variety of methods have been developed to perturb gene expression and protein abundance in specific tissues and/or at particular developmental stages of *C. elegans*. These include tissue-specific RNA interference (RNAi) (WATTS *et al.* 2020), conditional protein degradation (ZHANG *et al.* 2015; WANG *et al.* 2017; HILLS-MUCKEY *et al.* 2021) and site-specific recombinases (NANCE AND FROKJAER-JENSEN 2019; DRIESSCHAERT *et al.* 2021). Especially Cyclization recombination (Cre) and Flippase (FLP) enzymes are popular tools for the control of gene expression in a spatiotemporal manner (HUBBARD 2014; DRIESSCHAERT *et al.* 2021). While Cre was derived from the P1 bacteriophage (SAUER 1987), FLP originates from *Saccharomyces cerevisiae* (SENECOFF *et al.* 1985). The Cre and FLP recombinases recognize 34 bp sequences, that are called loxP (locus of crossing-over in P1) and FRT (FLP recognition target), respectively. DNA located between two target sequences is either excised or inverted depending on their orientation. Both systems have been used efficiently in *C. elegans*, for example to induce gene knockout (KO) (RUIJTENBERG AND VAN DEN HEUVEL 2015; KONIETZKA *et al.* 2020), control ectopic expression (SCHMITT *et al.* 2012), ablation of neurotransmission (DAVIS *et al.* 2008), determination of gene expression (GOMEZ-SALDIVAR *et al.* 2020), mapping of chromatin organization (CABIANCA *et al.* 2019; HARR *et al.* 2020) and transgenesis (NONET 2020). Moreover, by utilizing both Cre and FLP, further versatility and cell specificity can be achieved (GE *et al.* 2020; NONET 2020). Thanks to community efforts, a growing number of characterized and stable Cre and FLP drivers are available, which facilitates the development and implementation of recombination-based tools (VOUTEV AND HUBBARD 2008; KAGE-NAKADAI *et al.* 2014; RUIJTENBERG AND VAN DEN HEUVEL 2015; MUNOZ-JIMENEZ *et al.* 2017; MACIAS-LEON AND ASKJAER 2018; AYUSO AND ASKJAER 2019). Most recently, a light-inducible Cre recombinase has been added to the toolbox (DAVIS *et al.* 2021).

In some cases, the study of gene function at specific developmental time points can be compromised by remaining protein levels after gene perturbation. At a time point of interest, remaining protein might occlude the true phenotype associated with the gene's loss of function by RNAi or conditional KO. This may be particularly relevant for long-lived proteins, such as histones and nuclear pore complex (NPC) proteins, that sometimes show lifelong persistence (SAVAS *et al.* 2012; TOYAMA *et al.* 2013). Besides, re-initiation of translation in the case of frameshift-mediated KO appears to be more prevalent than previously anticipated (COHEN *et al.* 2019). The combination of gene KO methods with conditional protein degradation may help to overcome this hurdle and completely deplete protein levels.

Tools for targeted protein degradation are constantly being developed and adapted for *C. elegans* and other model organisms (NANCE AND FROKJAER-JENSEN 2019). Auxin-inducible degradation (AID) of proteins tagged with a 44 amino acid AID degron offers both temporal and spatial control through exposure to auxin and expression of *Arabidopsis thaliana* TIR1 protein, respectively (ZHANG *et al.* 2015). Wang et al. (WANG *et al.* 2017) developed a system for the degradation of green fluorescent protein (GFP)-tagged proteins in *C. elegans* building on previous protein depletion systems (CAUSSINUS *et al.* 2011; ARMENTI *et al.* 2014). In this GFP degradation (GFPdeg) system, a camelid single-domain antibody fragment that specifically binds GFP ("GFP nanobody") is fused to the SOCS-box adaptor protein ZIF-1, that recruits CUL-2/Cullin-2, an E3 ligase. This leads to ubiquitination and

proteasomal degradation of the GFP-tagged protein. An advantage of GFPdeg is that it is immediately applicable to any existing line expressing a GFP-tagged protein, but it offers only spatial control in its current version. Degradation kinetics in the AID or GFPdeg systems depend on the synthesis and turnover rates of the target protein, which sometimes renders protein depletion incomplete. Therefore, using AID or GFPdeg on its own may also not be sufficient for the inquiry of some biological processes and could benefit from the combination with genetic tools, such as site-specific recombination.

Here, we report an extension of the FLP-based toolbox for *C. elegans* by four means. Firstly, we describe novel integrated single-copy FLP drivers that efficiently induce recombination in the somatic gonad, distal tip cells, the P lineage or coelomocytes. We also report an improved FLP driver for intestinal cells and demonstrate that equally high recombination efficiency can be achieved for FLP drivers on different autosomes. These drivers increase the number of cell types amenable for easy FLP-mediated spatiotemporal control of gene expression. Secondly, we adapt the GFPdeg system for FLP-based regulation, thereby enabling spatiotemporal control of GFP fusion protein degradation. We show that inducible GFPdeg is equally efficient as the original constitutive version. Thirdly, using two endogenously GFP-tagged nuclear pore proteins, MEL-28/ELYS and NPP-2/NUP85, as test cases, we provide evidence that combined FLP-mediated gene KO and protein degradation is rapid and highly efficient to deplete stable proteins from a specific tissue of interest. The possibility of using a single FLP driver to control both conditional gene KO and protein degradation will facilitate the inquiry of tissue-specific gene function in complex biological processes. Lastly, we present the application of FLP-controlled RNA polymerase DamID (RAPID) (GOMEZ-SALDIVAR *et al.* 2020) for identification of transcribed genes in the hypodermis. We propose that combined with the growing list of tissue-specific FLP and Cre drivers, RAPID is an efficient and attractive method to explore transcription profiles across tissues without the need of physical isolation of cells.

Material and Methods

Plasmids

Promoter fragments for FLP expression constructs were PCR-amplified with *Pfu* polymerase using wild type *C. elegans* genomic DNA as template and inserted as *Not*I/*Kpn*I fragments into *Not*I/*Kpn*I of plasmid pBN338 (MUNOZ-JIMENEZ *et al.* 2017). Details are in Supplementary Tables S2 and S3. Exceptions were (1) pBN527 *gpa-14p::FLP::SL2::mNG* that was generated by first combining a 2.4 kb *Not*I/*Cla*I restriction fragment from pNP259 (SCHMITT *et al.* 2012) with a 0.6 kb *Cla*I/*Kpn*I PCR fragment followed by insertion into *Not*I/*Kpn*I of pBN338 and (2) pBN487 *unc-122p::FLP::SL2::mNG* that was generated by inserting a *Not*I/*BsrG*I PCR fragment into *Not*I/*Acc65*I of pBN338. For generation of pBN532 *hlh-12p::FLP::SL2::mTagBFP2*, an intergenic *gpd-2/-3* sequence was amplified with primers B1012 and B1364 (see Supplementary Table S1) using pBN338 as template. A sequence encoding mTag2BFP2 was amplified with B1365 and B1366 using pMINIT mTagBFP2 (PORTA-DE-LA-RIVA *et al.* 2021) as template. The two PCR fragments were PCR-stitched with primers B1012 and B1366 and inserted by NEBuilder HiFi DNA Assembly (New England Biolabs) into *Mlu*I of pBN523. To generate plasmids pBN548 *dat-1p::FLP::SL2::mNG* and pBN549 *hlh-*

140 *12p::FLP::SL2::mTagBFP2* for integration into universal MosSCI landing sites
141 (FROKJAER-JENSEN *et al.* 2014), *Xma*I/*Not*I fragments from pBN338 and pBN532,
142 respectively, were inserted into *Ngo*MIV/*Not*I of pBN8 (RODENAS *et al.* 2012).

143 Targeting plasmids for SapTrap CRISPR/Cas9 gene modification were obtained as
144 described (SCHWARTZ AND JORGENSEN 2016). Details for construction of plasmids
145 pBN309 *mCh::baf-1*, pBN433 *g>f>p::npp-2* (">" denotes an FRT site) and pBN493
146 *gf>p::baf-1* are provided in Supplementary Tables S1 and S3. The plasmids direct
147 the insertion of fluorescent tags immediately downstream of the endogenous start
148 codon. Plasmid pBN351 for insertion of *g>f>p* immediately upstream of the
149 endogenous *mel-28* start codon was generated from plasmids pMLS256, pMLS288
150 and pBN312 (SCHWARTZ AND JORGENSEN 2016; MUNOZ-JIMENEZ *et al.* 2017), sgRNA
151 oligonucleotides B1050 and B1051, 5' homology arm (499 bp; amplified with B1042
152 and B1043 using plasmid #1397 (GOMEZ-SALDIVAR *et al.* 2016) as template) and 3'
153 homology arm (258 bp; amplified with B1044 and B1045 using plasmid #1397 as
154 template) (see Supplementary Tables S1 and S3). Donor plasmid pBN477
155 containing FRT in the second *gfp* intron was constructed by inserting a 574 bp
156 *Xho*I/*Hin*dIII fragment from pBN312 into *Xho*I/*Hin*dIII of pMLS252 (SCHWARTZ AND
157 JORGENSEN 2016).

158 Plasmid pBN488 *hsp16.41p>mCh::his-58>vhhGFP4::zif-1* for targeted degradation
159 of GFP fusion proteins was constructed by amplifying *vhhGFP4::zif-1* with primers
160 B1333 and B1334 using plasmid pNH102 (a kind gift from Ngang Heok Tang and
161 Andrew Chisholm) as template. The PCR product was digested with *Xho*I and *Nhe*I
162 and inserted into plasmid pBN209 *hsp16.41p>mCh::his-58>dam::emr-1* (CABIANCA *et*
163 *al.* 2019) digested with the same enzymes to replace *dam::emr-1*.

164 Plasmid pBN537 *hsp16.41p>mCh::his-58>dam::rpb-6* for RAPID was constructed by
165 amplifying *rpb-6* with primers B1456 and B1457 using genomic DNA as template.
166 The PCR product was digested with *Ngo*MIV and *Nhe*I and inserted into plasmid
167 pBN209 digested with the same enzymes to replace *emr-1*.

168 *Nematode culture, strains and genome engineering*

169 Worm strains were maintained on Nematode Growth Medium (NGM) petri dishes
170 seeded with *Escherichia coli* OP50 (STIERNAGLE 2006). Unless otherwise noted,
171 strains were maintained at 16°C. The N2 strain was used as wild type reference.
172 Other strains are listed in Supplementary Table S4.

173 Single-copy insertion of FLP expression constructs into the *cxTi10882* locus on chrIV
174 or the *oxTi365* locus on chrV was done by microinjection into the gonads of EG6700
175 or EG8082 young adult hermaphrodites (FROKJAER-JENSEN *et al.* 2008; FROKJAER-
176 JENSEN *et al.* 2014; DOBRZYNSKA *et al.* 2016). Plasmids carrying FLP and *unc-119(+)*
177 as selection marker were injected at 50 ng/µl together with pCFJ601 *eft-3p::Mos1*
178 ((FROKJAER-JENSEN *et al.* 2012), 50 ng/µl), pBN1 *lmn-1p::mCh::his-58* ((RODENAS *et*
179 *al.* 2012), 10 ng/µl), pCFJ90 *myo-2p::mCh* ((FROKJAER-JENSEN *et al.* 2008), 2.5 ng/µl)
180 and pCFJ104 *myo-3p::mCh* ((FROKJAER-JENSEN *et al.* 2008), 5 ng/µl). Integration of
181 the FLP expression constructs was confirmed by detection of fluorescent
182 mNeonGreen (mNG) or mTagBFP2 in the target tissue of wild-type moving animals
183 without ectopic mCherry expression from the co-injection markers. For FLP
184 constructs without fluorescent co-expression markers, correct expression pattern
185 was confirmed after crossing with the dual-color FRT reporter (see Confocal
186 Microscopy below).

Similarly, single-copy insertion of vhhGFP4::ZIF-1 and Dam::RPB-6 expression constructs into the *ttTi5605* locus on chrII was done by microinjection into the gonads of EG4322 young adult hermaphrodites. Injection markers and transposase plasmid were injected at same concentrations as above. Integrity of the integrated transgenes was confirmed by PCR, and, after crossing to FLP drivers, functional assays (degradation of GFP fusion proteins for the GFPdeg system; see Confocal Microscopy below).

CRISPR/Cas9-mediated genome modification to generate strains BN581 *baf-1(bq13[mCh::baf-1])* III, BN1164 *baf-1(bq47[gf>p::baf-1])* III, BN902 *mel-28(bq17[g>f>p::mel-28])* III and BN1044 *npp-2(bq38[g>f>p::npp-2])* I was performed by microinjection of targeting plasmids pBN309, pBN493, pBN351 and pBN433, respectively, into the gonads of HT1593 *unc-119(ed3)* III young adult hermaphrodites (SCHWARTZ AND JORGENSEN 2016). Targeting plasmids were injected at 65 ng/µl together with plasmids #1286 *eft-3p::Cas9* ((FRIEDLAND *et al.* 2013), 25 ng/µl), pBN1 (10 ng/µl), pCFJ90 (2.5 ng/µl) and pCFJ104 (5 ng/µl). Successful modification of the target loci was confirmed by detection of fluorescent fusion proteins in the nuclear envelope throughout the body of wild-type moving animals without ectopic mCherry expression from the co-injection markers. The *unc-119(+)* selection marker was next excised by microinjection with Cre expression plasmid pMLS328 (SCHWARTZ AND JORGENSEN 2016). Finally, uncoordinated hermaphrodites were outcrossed to N2 males to remove the *unc-119(ed3)* allele.

Insertion of an FRT in the *baf-1* 3'-UTR was performed by microinjection of BN1164 *baf-1(bq47[gf>p::baf-1])* young adult hermaphrodites with a mixture containing 10 µM *baf-1* crRNA:trRNA duplex (B1312+B1067), 2.5 µM *dpy-10* crRNA:trRNA duplex (B1068+B1067), 3 µM recombinant Cas9, 4 µM *baf-1* ssDNA repair template (B1313) and 1 µM *dpy-10* ssDNA repair template (B725). Recombinant Cas9 was produced by the CABD Proteomics and Biochemistry Facility. All DNA and RNA oligonucleotides were purchased from IDT.

Confocal microscopy

To induce expression of either the dual-color FRT reporter or the GFPdeg system, NGM plates with nematodes were incubated for 15 min floating in a 34°C water bath. For evaluation of recombination efficiency and specificity, nematodes were left to recover at 20°C for 2-3 hours prior to imaging. For GFP degradation experiments, recovery was at 25°C for 1-24 hours as indicated for each experiment. For imaging, nematodes were anesthetized in 5 µl 10 mM levamisole HCl on 2% agarose pads and covered by a cover slip. Images were acquired with a Nikon Eclipse Ti microscope equipped with Plan Fluor 40×/1.3 and Plan Apo VC 60×/1.4 objectives and an A1R scanner using a pinhole of 1.2 airy units (MUNOZ-JIMENEZ *et al.* 2017). Cells with GFP signal as an indication of a recombination event in the dual-color reporter as well as mNG co-expression with FLP were evaluated from z-stacks acquired with the Nikon NIS software. To analyze the reduction of protein levels of GFP fusion proteins after FLP recombination and/or the induction of the GFP degradation system, specific regions and focal planes were localized to acquire reproducible sets of images. These are indicated in the text.

Fluorescence intensity was quantified in Fiji/ImageJ 2.1.0/1.53c (SCHINDELIN *et al.* 2012) by tracing and measuring the signal at the nuclear envelope with a freehand line of width 3. After subtracting the background measured in animals without expression of GFP, the data were analyzed in R Studio (1.3.1093 (TEAM 2020a);

running R 4.0.2 (TEAM 2020b)). Data were visualized either with base plotting or using ggplot2 (WICKHAM 2016), mainly within the ggpubr framework (version 0.4.0 (KASSAMBARA 2020)). For statistical analysis, Shapiro-Wilk test of normality and Levene's test for homogeneity of variance across groups were performed on the data sets to determine if either ANOVA and pair-wise t tests or Kruskal-Wallis rank sum test combined with Dunn's test for pairwise multiple comparisons of the ranked data were most suitable. In all cases, p values were adjusted for multiple comparisons (Benjamini & Hochberg method).

Brood size experiments

BN580 *g>f>p::baf-1*, BN1182 *mCh::baf-1/g>f>p::baf-1; nhx-2p::FLP* and BN1223 *mCh::baf-1/gf>p::baf-1>; nhx-2p::FLP* worms were cultured at 16°C until L4 larval stage. For BN1182 and BN1223, homozygous *mCh::baf-1*, *g>f>p::baf-1* and *gf>p::baf-1>* animals were selected under a fluorescence stereoscope. In each replica, 8-10 L4 larvae per strain were transferred to individual NGM plates and incubated at 20°C. During the reproductive period, adults were transferred to new plates each day and the numbers of progenies were recorded. Adults were censored if they desiccated on the walls of the plates or were damaged during transfer. Statistical analysis was done in R using Wilcoxon rank sum tests and adjusted for multiple comparisons (Benjamini & Hochberg method).

Lifespan experiments

Worms were cultured at 16°C until L4 larval stage. In each replica, 20 L4 larvae per strain were transferred to newly seeded NGM plates and incubated for 15 min floating in a 34°C water bath to induce the GFPdeg system. They were then continuously incubated at 25°C. During the reproductive period, the live adults were transferred to new plates each day to not confuse founders with their progeny. Throughout the experiment, the number of live and dead animals were recorded. Animals were censored if they disappeared, were damaged during transfer or died due to internal hatching. Statistical analysis was done in R using the survival package (version 3.2-7 (THERNEAU 2020)), which calculates Chi-square statistics based on a log-rank test.

RAPID

Worms were grown at 20°C for at least two generations on NGM plates seeded with *E. coli* GM119 *dam*- bacteria. Eggs were obtained by sodium hypochlorite treatment (STIERNAGLE 2006) and incubated in M9 containing 0.01% Tween-20 (M9-T) overnight at 20°C without food. For each strain and replica, four 100 mm NGM plates with a lawn of GM119 were seeded each with approximately 1000 synchronized L1 larvae and incubated at 20°C for 48 h until reaching L4 stage. Larvae were washed off the plates with M9-T, collected in 15 ml tubes and washed 8 times in M9-T. Next, worms were transferred to 1.5 ml tubes washed twice in M9-T. The supernatant was aspired to leave ~30 µl and tubes were snap frozen in liquid nitrogen and stored at -80°C until used.

To purify genomic DNA, samples were lysed in 5 freeze/thaw cycles (1 min in liquid nitrogen; 3 min in 37°C shaker) and processed with DNeasy Blood and Tissue Kit (QIAGEN #69504). Two hundred ng of genomic DNA was used as input in the DamID protocol that included an improved pool of AdR primers as described (DE LA CRUZ RUIZ *et al.* 2022). Dam-methylated fragments were amplified with 14 PCR cycles and quality checked on an Agilent Bioanalyzer 2100. Next, libraries were

282 prepared using 50 ng of PCR-amplified fragments and NEBNext® Ultra™ II DNA
283 Library Prep Kit for Illumina (E7645S). Library amplicons size range distribution was
284 checked as before, pooled and re-purified with 1x volume SpeedBeads (DE LA CRUZ
285 RUIZ *et al.* 2022) followed by sequencing at EMBL GeneCore using a NextSeq 500
286 (Illumina).

287 Sequencing fastq files were filtered to discard reads that do not start with the DamID
288 adapter followed by GATC ("CGCGGCCGAG*GATC*") using R Studio and the
289 damid.seq.R pipeline version 0.1.3 (available at github.com/damidseq/RDamIDSeq)
290 (SHARMA *et al.* 2016). Retained fragments were mapped to *C. elegans* UCSC
291 genome version ce11 with the same pipeline, which produced 9.5-41.9 million
292 uniquely mapped reads per sample. Normalization of Dam::RPB-6 reads to
293 GFP::Dam reads was performed using the damidseq_pipeline package
294 (https://owenjm.github.io/damidseq_pipeline/) (MARSHALL AND BRAND 2015) on the
295 bam files generated by the damid.seq.R script. Gene occupancy was computed as
296 log2(Dam::RPB-6/GFP::Dam) with polii.gene.call
297 (https://github.com/owenjm/polii.gene.call) using bedgraph output files from the
298 damidseq_pipeline and WBCel235 gene annotation. A false discovery rate (FDR) of
299 0.05 was used as threshold to call transcribed genes. Average profile plots and
300 heatmap were generated with SeqPlots (Version 3.0.12) using bedgraph output files
301 from the damidseq_pipeline and WBCel235 gene annotation; H3K36me3 signal
302 along either all protein coding genes or top20 transcribed genes on chromosome I
303 (included in the software) was used as comparison (STEMPOR AND AHRINGER 2016).
304 Genome browser views and Venn diagrams were generated with Integrative
305 Genomics Viewer (IGV Web App) (THORVALDSDOTTIR *et al.* 2013) and jvenn (Web
306 App) (BARDOU *et al.* 2014), respectively. Statistical significance of overlap between
307 protein coding gene lists was calculated with Fisher exact test for independence in
308 2x2 contingency tables using R Studio and a total count of protein coding genes of
309 19,975.

310 *Data availability*

311 See Table S1, Table S2, Table S3 and Table S4 for complete lists of primers,
312 promoters, plasmids and strains, respectively. Representative strains will be made
313 immediately available through the *Caenorhabditis* Genetics Center; plasmids and
314 other strains can be requested from the authors. Tables S5-S7 contain lists of
315 hypodermal genes identified by RAPID (Table S5), their overlap with other
316 hypodermal gene lists (Table S6) and their expression level in single-cell RNAseq
317 (Table S7). Raw and processed RAPID files are deposited at Gene Expression
318 Omnibus accession GSE214300 (https://www.ncbi.nlm.nih.gov/geo/).

319

320 **Results**

321 *Characterization of new FLP lines*

322 Previously, a series of efficient tissue-specific FLP-lines were generated by Mos1-
323 mediated Single Copy Insertion (MosSCI) (MUNOZ-JIMENEZ *et al.* 2017; MACIAS-LEON
324 AND ASKJAER 2018; AYUSO AND ASKJAER 2019; VAN DE WALLE *et al.* 2020). To expand
325 the existing toolkit, we created additional MosSCI lines that express FLP in specific
326 cell types and evaluated recombination efficiency with the heat-inducible dual color
327 reporter *bqSi294* that produces green nuclei (GFP::HIS-58) upon successful
328 recombination and red nuclei (mCherry::HIS-58) elsewhere (Figure 1A) (MUNOZ-

329 JIMENEZ *et al.* 2017). In most constructs (see below), an SL2 trans-splicing sequence
330 followed by the gene encoding the fluorescent protein mNeonGreen (mNG) was
331 inserted downstream of FLP (FLP::SL2::mNG), enabling visualization of FLP
332 expression by co-expression of mNG (MUNOZ-JIMENEZ *et al.* 2017).

333 We first generated a line that expresses FLP under control of the *ckb-3* promoter,
334 which is active in the Z1 and Z4 cells that compose the somatic gonadal primordium
335 of the hermaphrodite in early L1 larvae (KROETZ AND ZARKOWER 2015). When
336 crossed with the dual color reporter, we detected recombination in all 36 L1 larvae
337 analyzed; in 35 larvae both Z1 and Z4 expressed GFP::HIS-58, and one larva
338 expressed GFP::HIS-58 in a single cell (Figure 1B; Table 1). The majority of Z1/Z4
339 cells expressed GFP::HIS-58 only, indicating that recombination had taken place at
340 both alleles (67/72 cells = 93%), whereas both green and red histones were
341 observed in 4 cells. Of note, there were never more than the expected two green
342 nuclei at this developmental stage (early L1), which highlights the tissue specificity of
343 the *ckb-3p::FLP* line. The high efficiency of the line in the somatic gonadal
344 primordium implies that it is very suitable for manipulation of all five tissues of the
345 reproductive system: distal tip cells, gonadal sheath, spermatheca, spermatheca-
346 uterine valve and the uterus (Figure 1B) (HUBBARD AND GREENSTEIN 2005).

347 The distal tip cells (DTCs) play important roles during development as the leading
348 cells that guide migration of the gonad arms in hermaphrodites and also in control of
349 germ cell proliferation (HUBBARD AND GREENSTEIN 2005). To express FLP specifically
350 in DTCs, we used the *hlh-12* promoter which is expressed from L2 stage (TAMAI AND
351 NISHIWAKI 2007). We observed recombination in both DTCs in all hermaphrodites
352 analyzed (*n*=24, L2-adult stage; Figure 1B; Table 1). Except for one DTC in a young
353 L2 larva, recombination had taken place at both alleles (47/48 cells = 98%) and was
354 not observed in other cell types, demonstrating the high efficiency and specificity of
355 the *hlh-12p::FLP* line.

356 We then generated a *lin-31p::FLP* line to enable recombination in the vulval
357 precursor cells (VPCs). LIN-31 is expressed in P1.p-P11.p cells from the middle of
358 L1 stage, when these cells are born (TAN *et al.* 1998). We focused our attention on
359 the central VPCs in L2 larvae and on VPC descendants during vulval morphogenesis
360 in L3 and L4 larvae. Importantly, recombination of both alleles was observed in all
361 VPCs and VPC descendants in all animals (*n*=30, L2-adult stage; Figure 1B; Table
362 1). We also observed GFP::HIS-58 expression in a few head neurons, which is in
363 agreement with a previous report on *lin-31* expression (Supplementary Figure
364 S1A)(REECE-HOYES *et al.* 2007). Finally, we noted weak GFP::HIS-58 signal in hyp7
365 nuclei in late L3-L4 larvae, which we assume originates from fusion of descendants
366 of P3.p, P4.p and P8.p with the hyp7 syncytium (Supplementary Figure S1A).

367 In the first version of our FLP toolkit, we used the *elt-2* promoter to drive
368 recombination in the intestine with ~100% efficiency (MUNOZ-JIMENEZ *et al.* 2017).
369 However, because recombination was also detected in the somatic gonad, we
370 generated an alternative line based on the *nhx-2* promoter (NEHRKE AND MELVIN
371 2002). In young L1 larvae, the number of intestinal nuclei ranges from 19 to 22 and
372 increases to 30-34 in L2 larvae (MCGHEE 2007). Recombination efficiency reached
373 98% based on green-only nuclei and 100% when also including nuclei with
374 expression of both green and red histones (*n*=27, Figure 1B; Table 1). This
375 demonstrates high recombination efficiency, comparable to the *elt-2p::FLP* line.

376 Importantly, we did not detect recombination outside the intestine with the *nhx-*
377 *2p::FLP* line, so we recommend to use this line.

378 We next generated an *unc-122p::FLP* line to enable recombination in coelomocytes
379 (CCs), which are specialized cells thought to be involved in the innate immune
380 response and scavenging (LORIA *et al.* 2004; ALTUN AND HALL 2009). Two anterior
381 CC pairs are born during embryogenesis whereas a posterior pair is born right
382 before the L1/L2 molt. Consistently, in 8 of 8 L1s we observed 4 GFP::HIS-58
383 expressing CCs, and in 23 of 23 L3-L4 larvae 6 GFP::HIS-58 expressing CCs
384 (Figure 1B; Table 1). Expression of mCh::HIS-58 was not detected in the CCs,
385 indicating that both alleles had recombined, whereas GFP::HIS-58 expression was
386 restricted to the CCs.

387 We also attempted to generate additional lines to target specific neuronal subtypes,
388 including cholinergic neurons (using the *unc-17* promoter) and *gpa-14*-expressing
389 neurons. However, although both lines expressed the marker mNG in the expected
390 tissues, they also showed either recombination in unexpected cell types (for *unc-*
391 *17p::FLP*) or inefficient recombination (for *gpa-14p::FLP*) and were not characterized
392 in detail (Supplementary Figure S1B-C; see Discussion).

393 In the strains described above, co-expression of mNG serves to visualize when and
394 where FLP is expressed. However, in some experiments, the signal from mNG might
395 interfere with other fluorescent proteins. To circumvent this, we replaced mNG with
396 mTagBFP2 that emits blue light. When placed under control of the *hlh-12* promoter,
397 we observed mTagBFP2 expression and FLP-mediated recombination in both DTCs
398 of all animals (*n*=12; Supplementary Figure S1D). The sequences encoding mNG
399 and mTagBFP2 in the MosSCI plasmids are flanked by *Mlu*I restriction sites, which
400 facilitates the exchange of the former for the latter in the creation of new strains.

401 All lines described so far involve FLP expression constructs on chromosome IV. To
402 increase the versatility of the FLP toolkit, we subcloned *dat-1p::FLP* and *hlh-*
403 *12p::FLP* constructs to *ttTi5605* targeting vectors which enable insertion into
404 universal MosSCI sites on any autosome (FROKJAER-JENSEN *et al.* 2014). After
405 insertion of the FLP expression constructs on chromosome V we tested their
406 efficiency on the dual-color reporter and found that they both induce specific
407 recombination in all expected cells (Table 1). This suggests that other existing FLP
408 constructs can easily be adapted for insertion into different loci without compromising
409 their efficiency.

410

411 *Conditional gene knockout by GFP exon removal*

412 We previously designed a conditional knockout (KO) cassette based on GFP
413 containing FRT sites in introns 1 and 2 (Figure 2A) (MUNOZ-JIMENEZ *et al.* 2017).
414 Excision of GFP exon 2 by FLP causes a frame shift and a premature termination
415 codon, which most likely targets the mRNA for nonsense-mediated decay (ARRIBERE
416 *et al.* 2020). The premature termination codon precedes three short open reading
417 frames that are out of frame with respect to the gene downstream of GFP. Together,
418 this should completely prevent expression of the tagged protein. To test this
419 experimentally, we compared the consequence of either complete removal of the
420 *baf-1* gene (*gf>p::baf-1>*; "*>*" denotes the position of FRT; see Figure 2A) or removal
421 of GFP exon 2 in an endogenously tagged *gfp::baf-1* line (*g>f>p::baf-1*). BAF-1 is an
422 essential and ubiquitously expressed nuclear envelope protein (GORJANACZ *et al.*

423 2007). In both cases, we used the *nhx-2p::FLP* line described above to induce *baf-1*
424 KO specifically in intestinal cells, which negatively affects health (MUNOZ-JIMENEZ *et*
425 *al.* 2017). As controls we included (i) the *g>f>p::baf-1* line without FLP expression
426 and (ii) an endogenously tagged *mCh::baf-1* line without FRT sequences but with
427 FLP expression. While hermaphrodites of the two control lines produced an identical
428 number of progeny (*g>f>p::baf-1* 299±25 [mean±SD], n=10; *mCh::baf-1* 301±55,
429 n=15), fertility was reduced equally by 31% in the two conditional knockout lines
430 (*g>f>p::baf-1; nhx-2p::FLP* 207±71, n=15; *gf>p::baf-1>; nhx-2p::FLP* 206±68,
431 n=12)(Figure 2B). Based on this, we conclude that excision of the second exon of
432 the GFP KO cassette causes an equally strong loss of function phenotype as
433 complete gene removal. Moreover, it provides the advantage that insertion of the
434 GFP KO cassette in the 5'-end of a target gene in a single step is easier than
435 inserting both a GFP tag (with a single FRT) and a second FRT inside or
436 downstream of the gene.

437 While conditional gene KO prevents synthesis of new transcripts, mRNA and protein
438 molecules already existing in the cell might persist for days, weeks or even months
439 (TOYAMA *et al.* 2013). This may obscure both investigation of gene function and
440 potential therapeutic interventions. To address this, we evaluated the kinetics of
441 GFP::MEL-28 depletion from hypodermal cells of *g>f>p::mel-28; dpy-7p::FLP*
442 hermaphrodites. MEL-28 is a component of the long-lived NUP107 nuclear pore
443 subcomplex and is required for DNA segregation and post-mitotic nuclear assembly
444 (FERNANDEZ AND PIANO 2006; GALY *et al.* 2006; TOYAMA *et al.* 2013). Although the
445 *dpy-7* promoter is active already during embryogenesis to drive FLP expression,
446 ~95% of GFP::MEL-28 was still present in L1 larvae as compared to the control
447 *g>f>p::mel-28* line without FLP expression (Figure 3; compare Control and KO in
448 3B). In contrast, in L2 larvae and young adults a dramatic reduction of the median
449 GFP::MEL-28 signal to ~12% and ~3%, respectively, was observed specifically in
450 the hypodermis (Figure 3). This demonstrates the potential of conditional KO
451 methods to evaluate the function of long-lived proteins in late larvae and adults (see
452 also below), whereas they might be less suitable in early larvae.

453

454 *FLP-mediated protein degradation*

455 To enable analysis of long-lived proteins during development, we developed a
456 system for FLP-mediated, inducible and rapid protein degradation from specific cells.
457 A potent system for constitutive tissue-specific degradation of GFP-tagged proteins
458 based on expression of vhhGFP4::ZIF-1, a GFP-binding nanobody fused to ZIF-1,
459 was recently developed in *C. elegans* (WANG *et al.* 2017). To achieve both temporal
460 and spatial control of degradation of GFP-tagged proteins (hereafter termed
461 GFPdeg), we replaced the *gfp::his-58* sequence of the dual color reporter with a
462 sequence encoding vhhGFP4::ZIF-1. In this design, tissue-specificity is controlled by
463 the choice of a particular FLP-expressing line, whereas temporal control is provided
464 by the heat-inducible *hsp-16.41* promoter (Figure 4A).

465 We first determined that basal expression from the *hsp-16.41* promoter in the
466 absence of heat induction does not cause depletion of GFP::MEL-28 in the
467 hypodermis (Figure 4B). This implies that the system can be used to evaluate the
468 function of essential proteins late in development by raising the animals at 16°C until
469 induction. We next investigated whether the heat-induced GFPdeg system is equally
470 efficient as the original constitutive variant (WANG *et al.* 2017). We focused on

471 degradation of GFP::MEL-28 in intestinal cells. GFP intensity was quantified in one
472 or two intestinal cells closest to the pharynx and to the microscope lens to ensure
473 consistent measurements. Other intestinal cells often lie below the gonad, impeding
474 reproducible quantification. Three hours after a short heat pulse (15 min; 34°C) the
475 median GFP::MEL-28 intensity was reduced to ~27% in the inducible GFPdeg strain,
476 whereas slightly less protein remained in the constitutive GFPdeg strain (~18%;
477 Figure 4C, left graph). By exposing the animals to two 15 min heat pulses at 34°C,
478 one 24h and another 3h prior to imaging, the efficiencies of the inducible and
479 constitutive GFPdeg systems were equal (p=0.91; Figure 4C, right graph; Figure
480 4D). This demonstrates, that additional temporal control of the tissue-specific
481 GFPdeg module can be achieved without compromising degradation efficiency.
482 Depending on the protein of interest, induction conditions may have to be optimized.
483 For instance, the efficiency of endogenous GFP::MEL-28 degradation in the intestine
484 by either the constitutive or the inducible system (Figure 4C-D) is lower than the
485 depletion reported for endogenous GFP::MDF-1 based on the identical constitutive
486 GFPdeg strain (WANG *et al.* 2017). To evaluate the degradation dynamics in more
487 details, we measured GFP::MEL-28 levels in hypodermal cells at different time
488 frames after a single induction of GFPdeg (15 min; 34°C). Hypodermis-specific
489 expression of vhhGFP4::zif-1 was ensured by excision of *mCh::his-58* with FLP
490 under the control of the *dpy-7* promoter. All images were taken from a region of the
491 hypodermis closest to the lens and just posterior to the pharynx. One hour after
492 induction, the median level of GFP::MEL-28 was reduced to ~55% and further down
493 to ~19-20% after 2-4 h (Figure 5). A possible explanation for the remaining
494 GFP::MEL-28 even at the optimal time points (2-4 h) could be novel protein
495 synthesis since the degradation system will only be active for a finite time after
496 induction. Indeed, substantial protein re-synthesis was observed 24 h after heat
497 shock (Figure 5). The time frame of optimal degradation efficiency allows some
498 flexibility in protocol design. However, these protocols, especially number and timing
499 of heat inductions, presumably need to be tailored to the protein of interest and its
500 turnover.

501

502 *Combination of FLP-mediated gene knockout and protein degradation*

503 Having available two FLP-controlled systems for inhibition of protein expression, we
504 decided to test the efficiency of combining them. In this setup, the same FLP driver
505 controls both conditional gene KO and protein degradation (Figure 6A). As a proof of
506 principle, we evaluated the combined action of the GFP KO cassette and GFPdeg on
507 the expression of endogenously GFP-tagged MEL-28 in the hypodermis. GFPdeg
508 was induced by exposing young L1s to a short heat pulse (15 min; 34°C) followed by
509 incubation at 16°C. The effect was first evaluated in L1 larvae after 3 h and again in
510 L2 larvae as well as young adults. In contrast to the GFP KO system which alone
511 had insignificant effects in L1 larvae, the combination of the two systems led to
512 ~80% reduction of median GFP::MEL-28 signal (Figure 3). In L2 larvae, GFP::MEL-
513 28 levels in the hypodermis were further decreased to ~3% and undetectable in most
514 young adults. Thus, in all three life stages tested, the combination of conditional
515 gene knockout and protein degradation provided the most efficient inhibition of
516 protein expression. We also compared the efficiency of either conditional gene KO
517 alone or in combination with targeted protein degradation by inserting the GFP KO
518 cassette in frame after the start codon of another stable nuclear pore protein, NPP-

519 2/NUP85. In young adults, the conditional KO caused a reduction of ~97% of
520 GFP::NPP-2 in the hypodermis, whereas only ~1.5% remained when conditional KO
521 was combined with the GFPdeg system (Figure 6B-C).

522 To test if these dramatic reductions of endogenous GFP::NPP-2 in the hypodermis
523 had consequences on the health of the animals, we determined their lifespan at
524 25°C. We followed >175 animals for each genotype and observed a 22-33%
525 reduction in median lifespan from 9 days post L4 in GFP::NPP-2 control animals
526 (95% confidence interval [CI] = 9-10 days) to 7 days in conditional KO animals (95%
527 CI = 6-7 days) and to 6 days in animals with combined conditional KO and GFPdeg
528 systems (95% CI = 6-7 days) (Figure 6D. Expression of FLP and GFPdeg in the
529 absence of the GFP KO cassette had no effect on the lifespan (p=0.3). The
530 statistically insignificant shift to the left of the lifespan curve for the animals with the
531 combined conditional KO and GFPdeg (red line) as compared to the animals with the
532 conditional KO only (dark red line; p=0.5) is in line with the unsubstantial difference
533 in GFP::NPP-2 signal intensity between the two strains. We conclude that conditional
534 NPP-2 KO in the hypodermis causes a dramatic shortening of lifespan, illustrating
535 the suitability of the combination of the GFP KO cassette and the GFPdeg system for
536 evaluation of physiological consequences of protein depletion in specific tissues.

537

538 *Tissue-specific transcriptomic profiling by RAPID*

539 Various complementary methods are available for identification of gene expression
540 profiles in specific cell types in *C. elegans*, including physical isolation of cells or
541 nuclei of interest (HAENNI *et al.* 2012; STEINER *et al.* 2012; KALETSKY *et al.* 2018),
542 affinity purification of RNAs from specific cells (BLAZIE *et al.* 2017), trans-splicing-
543 based RNA tagging (MA *et al.* 2016), and mapping of RNA polymerase occupancy
544 (GOMEZ-SALDIVAR *et al.* 2020; KATSANOS *et al.* 2021). RNA polymerase DamID
545 (RAPID) (GOMEZ-SALDIVAR *et al.* 2020) and Targeted DamID (TaDa) (KATSANOS *et al.*
546 2021) are based on tissue-specific basal expression of *E. coli* Dam
547 methyltransferase fused to the RNA polymerase subunit RPB-6. The Dam::RPB-6
548 fusion protein provides an *in vivo* footprint of RNA polymerases on transcribed genes
549 by specific methylation of GATC sequences that are identified by enzymatic and
550 deep sequencing techniques (MARSHALL *et al.* 2016; ASKJAER AND HARR 2021).

551 RAPID relies on recombinases to achieve tissue specificity and has been used in
552 body wall muscles, intestine and specific neurons (GOMEZ-SALDIVAR *et al.* 2020). To
553 increase the number of tissues immediately amenable to RAPID, we adapted it for
554 FLP-mediated spatiotemporal control. We cloned and inserted a *dam::rpb-6* fusion
555 gene downstream of the FRT-flanked *mCh::his-58* cassette used above and under
556 control of the *hsp-16.41* promoter (Figure 7A). We introduced a single copy of this
557 construct into the *C. elegans* genome and crossed the resulting line with a *dpy-*
558 *7p::FLP* driver. Nematodes were cultured at 20°C to ensure low levels of Dam::RPB-
559 6 expression in the hypodermis and total genomic DNA was purified from L4 larvae.
560 DNA from animals expressing GFP::Dam was used to control for unspecific
561 methylation. The genome-wide association profile of Dam::RPB-6 was determined
562 by deep sequencing (see Materials and Methods), which revealed a list of 2331
563 protein coding genes with FDR < 0.05 (Table S5). When plotting the RAPID signal
564 along all protein coding genes, an increase in signal is observed from the
565 transcriptional start site (TSS) to the transcriptional end site (TES), similar to
566 previous RAPID and TaDa observations (GOMEZ-SALDIVAR *et al.* 2020; KATSANOS *et*

567 *al.* 2021)(Figure 7B, left). However, clustering the signal from individual genes using
568 k-means algorithm (with default number of clusters = 5 (STEMPOR AND AHRINGER
569 2016)) suggests that the average signal masks multiple different patterns of RAPID
570 signal along genes (Figure 7B, middle). A more uniform RAPID signal from TSS to
571 TES is also observed when averaging the 2331 genes determined as expressed in
572 the hypodermis with FDR < 0.05 (Figure 7B, right). Among the transcribed genes are
573 several known and expected hypodermal genes, such as *col-39*, *col-79*, *col-80* and
574 *sqt-1* that express collagens as well as ubiquitously expressed genes *eef-1A.1* and
575 *fib-1* (Figure 7C).

576 To evaluate the specificity of RAPID, we compared the list of 2331 transcribed genes
577 to three datasets of genes reported to be expressed in the hypodermis (BLAZIE *et al.*
578 2017; KALETSKY *et al.* 2018; KATSANOS *et al.* 2021) (Figure 7C-D; Table S6). Our list
579 overlapped significantly with each of the individual datasets (54-66% overlap;
580 p<2.2e-16 Fisher's exact test), and 1860 genes (80%) overlapped with at least one
581 of the three datasets. These overlaps are comparable to those observed when
582 comparing the three other datasets among each other (Figure 7D). Moreover, when
583 exploring a small arbitrarily chosen subset of the 471 genes not overlapping with any
584 of the three other datasets, at least 22/50 (44%) are reliably detected in hypodermal
585 cells in single cell RNAseq performed on embryos (PACKER *et al.* 2019) (Table S7).
586 This argues that many of the genes identified uniquely by RAPID are expressed in
587 the hypodermal lineage during development. We conclude that RAPID is an
588 attractive and versatile method to identify transcribed genes in specific tissues with
589 high confidence.

590

591 **Discussion**

592 An increasing number of specific and efficient FLP and Cre drivers generated by the
593 *C. elegans* community are facilitating a variety of precise functional assays to
594 interrogate neural circuits (DAVIS *et al.* 2008; SCHMITT *et al.* 2012; KONIETZKA *et al.*
595 2020; DAVIS *et al.* 2021), cell proliferation and differentiation (RUIJTENBERG AND VAN
596 DEN HEUVEL 2015), gene expression programs (GOMEZ-SALDIVAR *et al.* 2020; VAN DE
597 WALLE *et al.* 2020) and chromatin organization (CABIANCA *et al.* 2019; HARR *et al.*
598 2020). In this study, we report four new FLP lines that reliably induce recombination
599 specifically in either distal tip cells, the somatic gonad, coelomocytes or in epithelial
600 Pn.p cells. The efficiency of recombination was ~100% in all animals evaluated for
601 the four lines. We also demonstrate that similarly high recombination efficiency is
602 achieved when FLP is expressed from single-copy transgenes on different
603 autosomes. In the case of the *ckb-3p::FLP* line, recombination was observed already
604 in the earliest progenitors Z1 and Z4, which implies that the line is suitable to target
605 all cell types of the somatic gonad, including distal tip cells, gonadal sheath,
606 spermatheca, spermatheca-uterine valve and the uterus (HUBBARD AND GREENSTEIN
607 2005). In contrast, the activity of the *hlh-12p::FLP* line is restricted to the distal tip cell
608 and may thus be useful to investigate its stem cell niche function (KIMBLE AND SEIDEL
609 2008). Similarly, biological processes in coelomocytes are amenable to manipulation
610 by the *unc-122p::FLP* line, whereas the *lin-31p::FLP* line induces recombination in
611 the cells producing the vulva. We previously created a FLP line to induce
612 recombination in intestinal cells based on the *elt-2* promoter. However, because this
613 promoter can also drive expression in other tissues (RUIJTENBERG AND VAN DEN
614 HEUVEL 2015; MUNOZ-JIMENEZ *et al.* 2017), we developed here a novel line based on

615 the *nhx-2* promoter. The new line is equally efficient to produce recombination in the
616 intestine (Table 1) and with the advantage of not provoking recombination
617 elsewhere. We also attempted to construct lines for specific neurons using the
618 promoters of *gpa-14* and *unc-17*. In the case of *gpa-14*, we observed variable
619 recombination rates in FLP-expressing cells (0, 1 or 2 alleles of the single-copy
620 reporter). It seems that the behavior of the specific cells is reproducible between
621 individuals, but we do not know if this is due to differences in FLP expression levels
622 and/or the FRT sites being less accessible in certain cells. For the *unc-17p::FLP* line,
623 we observed widespread recombination in cholinergic neurons as expected but also
624 in the hypodermis. We speculate that this could be due to an inability of our construct
625 to precisely reflect *unc-17* expression (PEREIRA *et al.* 2015), although we also note
626 that two cholinergic neurons, PVNL and PVNR, are sister cells to two hypodermal
627 cells (TLappa and TRappa). Thus, if *unc-17p::FLP* is activated already in the
628 progenitor cells TLapp and TRapp, GFP::HIS-58 expression would be expected in
629 both cell types.

630 We previously proposed that inserting a GFP KO cassette (with FRT sites in *gfp*
631 introns 1 and 2) immediately after the start codon of a gene provides an informative
632 GFP fusion protein and a conditional KO allele in a single step (MUNOZ-JIMENEZ *et al.*
633 2017). In this study we have further validated this approach by comparing strains
634 that either carry the GFP KO cassette in the endogenous *baf-1* locus or a GFP
635 cassette with a single FRT and a second FRT downstream of *baf-1*. When combined
636 with an *nhx-2p::FLP* driver to KO *baf-1* specifically in the intestine, identical
637 reductions of fertility were detected in the two strains. Furthermore, using the GFP
638 KO cassette, we determined that conditional KO of *npp-2*/NUP85 in the hypodermis
639 caused a dramatic lifespan shortening. We therefore conclude that insertion of the
640 GFP KO cassette into an endogenous locus by CRISPR provides an attractive dual
641 tool to study protein dynamics and KO phenotypes in a single workflow. A limitation
642 of the approach is that the GFP KO cassette should be inserted in the 5'-end of the
643 open reading frame. As with other gene tagging experiments, tests for hypomorph
644 phenotypes should be performed.

645 Although gene KO is often considered an ultimate test for gene function, slow mRNA
646 and protein turnover can delay the appearance of loss-of-function phenotypes. This
647 is particularly relevant for organisms with rapid development and relatively short
648 lifespan, such as *C. elegans*. Moreover, the irreversible nature of gene KO may be
649 disadvantageous in some experimental designs. Targeted protein degradation is a
650 relevant alternative and auxin-inducible degradation (AID) stands out as an attractive
651 and popular option due to its fast kinetics and both inducible and reversible nature
652 (ZHANG *et al.* 2015). Concerns have been raised regarding auxin-independent
653 depletion of AID-tagged proteins (see references in (NANCE AND FROKJAER-JENSEN
654 2019)) and potential effects of auxin on endoplasmic reticulum stress (BHOI *et al.*
655 2021), but recent optimization of AID tools may have overcome this (HILLS-MUCKEY
656 *et al.* 2021). We show here that GFPdeg, an alternative protein degradation system
657 based on a GFP-binding nanobody (WANG *et al.* 2017) and adapted for FLP-
658 mediated spatiotemporal control, can efficiently deplete 80% of a long-lived nuclear
659 pore protein, MEL-28/ELYS, fused to GFP. By comparing the degradation of
660 GFP::MEL-28 in intestinal cells using either the original, constitutive version of
661 GFPdeg (WANG *et al.* 2017) or the heat inducible version of GFPdeg developed in
662 this study, we conclude that they are equally efficient. Importantly, the GFPdeg
663 system is immediately applicable to study the function of any GFP-tagged fusion

664 protein. We chose to focus on stable nuclear pore proteins (SAVAS *et al.* 2012;
665 TOYAMA *et al.* 2013) in our study as they are probably more challenging to deplete
666 but we assume that higher depletion efficiencies will be observed for proteins with
667 shorter half-lives. The original GFPdeg version (WANG *et al.* 2017) has the
668 advantage that it involves only two components (GFP-tagged fusion protein and
669 constitutive, tissue-specific GFPdeg) and does not require induction. In contrast, our
670 FLP-based GFPdeg system includes three components (GFP-tagged fusion protein,
671 tissue-specific FLP driver and heat-inducible, FRT-flanked GFPdeg) and requires
672 one or two short 15 min exposures to 34°C. On the other hand, our inducible system
673 allows to evaluate processes at any stage in development or during aging by raising
674 the nematodes at standard temperatures until induction at the desired time point.
675 This cannot be achieved with the constitutive system where the animal's
676 development potentially arrests once the concentration of the target protein is below
677 a required threshold. We envision that the FLP-controlled GFPdeg system can be
678 further modified to incorporate other inducers (MONSALVE *et al.* 2019; WURMTHALER
679 *et al.* 2019; DRIESSCHAERT *et al.* 2021) in situations where short heat pulses are
680 incompatible with the experimental design.

681 Depending on the experimental setup, either site-specific gene KO or targeted
682 protein degradation may be sufficient to elucidate gene function. However, bimodal
683 control of protein levels may be particularly valuable for the study of long-lived
684 proteins during early developmental stages as highlighted in this study. By
685 combining the GFP KO cassette and the GFPdeg system, we have generated a
686 protocol that provides two-fold control of tissue-specific protein depletion. On one
687 hand, a specific FLP driver induces gene KO in a tissue of interest and thus prevents
688 synthesis of mRNA from the target gene. On the other hand, the same FLP driver
689 excises tissue-specifically the FRT-flanked *mCh::his-58* cassette from the GFPdeg
690 construct, thus enabling heat-induced and rapid degradation of existing GFP-tagged
691 target protein. We show that the combined KO and GFPdeg systems can deplete
692 GFP::MEL-28 and GFP::NPP-2 to non-detectable levels, thus offering a highly
693 efficient approach for spatiotemporal control of protein levels in a multicellular
694 organism.

695 One of the strengths of recombinase-based genome engineering is its versatility: the
696 possibility of using collections of stable FLP and Cre drivers to control a variety of
697 different effectors through straight-forward genetic crosses (HUBBARD 2014; NANCE
698 AND FROKJAER-JENSEN 2019; DRIESSCHAERT *et al.* 2021). The Cre/loxP system was
699 recently utilized to generate tissue-specific transcription footprints by RNA
700 polymerase DamID (RAPID) in *C. elegans* (GOMEZ-SALDIVAR *et al.* 2020). In RAPID
701 and other DamID methods for transcriptional profiling *E. coli* Dam is fused to an RNA
702 polymerase subunit and expressed at low levels to mark *in vivo* transcribed genes
703 (SOUTHALL *et al.* 2013; ASKJAER AND HARR 2021). In this study we have widened the
704 range of tissues immediately accessible to RAPID by adapting RAPID for FLP-
705 mediated spatial control. We have validated the potential of RAPID in *C. elegans* by
706 expressing Dam::RPB-6/POLR2F specifically in the hypodermal lineage through the
707 use of a *dpy-7p::FLP* driver and identified 2331 transcribed genes. We compared our
708 list with hypodermal data from another recent DamID-based (TaDa) study (KATSANOS
709 *et al.* 2021) and two RNAseq-based studies (BLAZIE *et al.* 2017; KALETSKY *et al.*
710 2018) and found a significant overlap in all cases ($p<2.2e-16$). We propose that the
711 set of 847 protein coding genes identified in all four studies (Table S6) can be
712 considered a high-confidence transcriptional signature of the hypodermis. A pilot

comparison of genes found uniquely in RAPID (i.e. not confirmed by any of the three other methods) revealed a relevant overlap with genes detected in hypodermal cells by single-cell RNA-seq (PACKER *et al.* 2019), suggesting that many of the unique RAPID genes are true positive hits.

Although the overlap between the gene lists identified in our RAPID experiment and the TaDa study is much higher than would be expected by chance, ~50% of the genes identified in one study were not found in the other. In both cases, Dam::RPB-6 was used to mark transcribed genes and samples were prepared at the L4 stage so how can the many unique genes be explained? An important difference is that Katsanos and co-workers used a mutated version of the *dpy-7* promoter ("*dpy7syn1*") for TaDa in the hypodermis to avoid signal from seam cells (KATSANOS *et al.* 2021), whereas we used a wild type *dpy-7p* sequence to drive FLP expression (MUNOZ-JIMENEZ *et al.* 2017). Katsanos and co-workers also determined the transcriptomic profile for seam cells and found that ~1/3 of the genes in their hypodermis and seam cell datasets are unique (KATSANOS *et al.* 2021). Our RAPID gene list overlaps significantly with both the entire seam cell gene list (1013 overlapping genes; $p<2.2e-16$) and the unique seam cell gene list (106 overlapping genes; $p=0.016$), suggesting that part of the RAPID signal in our experiments is derived from seam cells (Figure S2). It should be noted that the lineages of the two cell types are interconnected because many of the daughter cells from dividing seam cell precursors fuse with the hypodermis during larval development. Differences in the protocols for preparation of deep sequencing libraries (sequences of adapters, PCR conditions, +/- removal of adapters and fragmentation, etc.) are also likely to introduce variation in the lists of identified genes. Finally, the strategies underlying tissue specificity is also different between RAPID and TaDa (ASKJAER AND HARR 2021). Spatial control of basal Dam::RPB-6 expression is achieved in RAPID by combining FLP or Cre-mediated genome recombination with a non-induced *hsp* promoter (Figure 7A), whereas TaDa is based on a tissue-specific promoter and translation re-initiation of a bicistronic mRNA containing an upstream open reading frame and *Dam::rpb-6* separated by one or several stop codons. TaDa is feasible with a single transgene whereas RAPID relies on a recombinase transgene and a *Dam::rpb-6* transgene typically integrated on separate chromosomes. Although this appears to favor TaDa versus RAPID, the growing list of stable and efficient FLP and Cre drivers implies that different tissues can be explored with RAPID through a simple cross to combine the recombinase and *Dam::rpb-6* transgenes. In contrast, TaDa requires the design, cloning and transgenesis for each new cell type to be analyzed.

Because the methylation on GATC by Dam is only erased when cells enter S phase and replicate their DNA, RAPID and TaDa provide the history of transcription during the life of the cell. PATseq and FACS produce instead a compilation of all mRNAs present in the cell at the time of harvest. Depending on the biological question to be addressed, a particular method might be most suitable. The PATseq and FACS studies report the largest hypodermal gene sets (BLAZIE *et al.* 2017; KALETSKY *et al.* 2018), but they also suffer higher intrinsic risks of including false positive hits. For instance, FACS isolation of a particular cell type might include contaminants in the form of cells from other tissues. Similarly, in the PATseq protocol, mRNA from unlabeled cells might potentially co-purify with the mRNA from the target cells. Such false positives are difficult to control for in the FACS and PATseq protocols. In contrast, RAPID and TaDa are based on isolation of genomic DNA from the entire

762 organism followed by amplification of methylated GATC fragments from a tissue of
763 interest, library preparation and a statistical analysis to identify genes with a higher
764 Dam::RPB-6/GFP::Dam methylation ratio. Importantly, although the signal from
765 Dam::RPB-6 reflects RNA polymerase occupancy on transcribed genes rather than
766 transcription itself, the signal intensity correlates with transcript abundance
767 (SOUTHALL *et al.* 2013; GOMEZ-SALDIVAR *et al.* 2020; KATSANOS *et al.* 2021).
768 Furthermore, comparing Dam::RPB-6 methylation values across experimental
769 conditions enables identification of differentially expressed genes (WIDMER *et al.*
770 2018).

771 We conclude that FLP-controlled RAPID has the capacity to identify transcribed
772 genes in a tissue of interest with high confidence. We have tested the method in the
773 hypodermis, but it is easily applied to other cell types for which an appropriate FLP
774 driver is available. In particular, we envision that RAPID will be advantageous for cell
775 types that are hard to isolate in an intact state, such as neurons (GOMEZ-SALDIVAR *et*
776 *al.* 2020).

777

778 **Table 1 Efficiency of FLP-mediated recombination**

Promoter[a]	Cell type	Stage[b]	Observed[c]	Expected	Efficiency
ckb-3	Somatic gonad	Early L1	2.0±0.2 (36)	2	99%
dat-1	Dopaminergic neurons	L3-L4	8.0±0.0 (11)	8	100%
hlh-12	Distal tip cell	L2-adult	2.0±0.0 (24; chrIV[a]) 2.0±0.0 (10; chrV[a])	2	100%
lin-31	P1.p-P11.p (P5.p-P7p)	L2-L4	3.0±0.0 (14)	3[d]	100%
		L3	12.0±0.0 (13)	12[d]	100%
		L4	22.0±0.0 (3)	22[d]	100%
nhx-2	Intestine	L1	20.0±0.0 (10)	20 (19-22)	100%
		L2	31.9±0.6 (17)	32 (19-22)	100%
unc-122	Coelomocytes	L1	4.0±0.0 (8)	4	100%
		L3-L4	6.0±0.0 (23)	6	100%

779 [a] Single-copy FLP constructs inserted on chrIV except *dat-1p::FLP* and one of the
780 *hlp-12p::FLP* constructs that were inserted on chrV.

781 [b] Developmental stage that was used for determination of recombination efficiency.

782 [c] Average number of GFP positive nuclei ± SD; number in brackets: *n*.

783 [d] Efficiencies were calculated based on recombination in central Pn.p cells and their
784 descendants.

785

786 **Acknowledgments**

We are grateful to Andrew Chisholm, Carmen Ortiz González, Michael Krieg, Montserrat Porta, Ngang Heok Tang, Patricia Regina Rider García and Sara Castaño Díaz for reagents and advice. We also wish to acknowledge Ana Miñan Fernández from the CABD Functional Genomics Facility for microinjections, Laura Tomás from the CABD Proteomics and Biochemistry Facility for recombinant proteins, Katherina García from the CABD Imaging Facility for technical assistance; the Caenorhabditis Genetics Center (CGC), which is funded by the National Institutes of Health (NIH) Office of Research Infrastructure Programs (P40 OD010440) and WormBase. This project was funded by the Spanish State Research Agency and the European Regional Development Fund (BFU2016-79313-P, CEX2020-001088-M and PID2019-105069GB-I00).

Figure legends

Figure 1. Characterization of novel FLP lines. (A) Schematic representation of the dual color reporter used to evaluate recombination activity. Upon temperature induction of the *hsp-16.41* promoter, the reporter expresses red (mCh) or green (GFP) histone HIS-58 in cell lineages without or with FLP-mediated recombination, respectively. (B) Evaluation of FLP lines crossed with the dual color reporter. Although the FLP lines co-express diffuse mNG in the cytoplasm, GFP::HIS-58 is clearly visible in the expected nuclei. (Ba) *ckb-3p::FLP::SL2::mNG*: maximum projections of 2-3 confocal sections of BN854 L1 larva (Ba') and larva at L3/L4 molt (Ba''). The Z1 and Z4 somatic gonad precursor cells are indicated. (Bb) *hlh-12p::FLP::SL2::mNG*: single confocal sections of BN1204 L2 larva (Bb') and young adult (Bb''). The distal tip cells (DTCs) are indicated. (Bc) *lin-31p::FLP::SL2::mNG*: maximum projections of three confocal sections of BN1023 L2 larva (Bc') and L4 larva (Bc''). The posterior daughters of P1-P7 and vulA-vulF forming the vulva are indicated. (Bd) *nhx-2p::FLP::SL2::mNG*: maximum projection of five confocal sections of BN999 L1 larva (Bd'; indicated area shown enlarged in Bd''). (Be) *unc-122p::FLP::SL2::mNG*: maximum projections of four confocal sections of BN1029 L1 larva (Be') and L4 larva (Be''). The three pairs of coelomocytes are indicated. Scale bars 10 µm.

Figure 2. Comparison of GFP KO cassette and complete gene KO. (A) Schematic representation of the two KO strategies. In the first strategy (top), a GFP KO cassette with FRTs in *gfp* introns 1 and 2 is inserted immediately downstream of, and in frame with, the start codon of a gene of interest (here *baf-1*). FLP-mediated recombination leads to a frame shift and a premature termination codon ("Stop"). In case the ribosome remains associated with the mRNA, the three downstream open reading frames are all out-of-frame with *baf-1* (purple lines). In the second strategy (bottom), the GFP cassette contains a single FRT and a second FRT is inserted in the 3'-UTR of the gene of interest. FLP-mediated recombination leads to complete gene removal. (B) Brood sizes were determined for control animals (*g>f>p::baf-1* and *mCh::baf-1; nhx-2p::FLP*) and for animals with conditional KO of *baf-1* in the intestine (*g>f>p::baf-1; nhx-2p::FLP* [first strategy] and *gf>p::baf-1>; nhx-2p::FLP* [second strategy]; strains BN580, BN1182 and BN1223). Each point represents the number of progenies produced by an individual worm; *n* for each genotype is indicated in parentheses. P values from pair-wise t tests and adjusted for multiple comparisons (Benjamini & Hochberg method) are indicated. In these and subsequent boxplots, the midline represents the median and the upper and lower

835 limits of the box correspond to the third and first quartile, respectively. The whiskers
836 extend to the lowest and higher observations but maximum up to 1.5 times the
837 interquartile range.

838 Figure 3. KO of GFP::MEL-28 in hypodermal nuclei. (A) Confocal micrographs of
839 *g>f>p::mel-28* L1 larvae, L2 larvae and young adults either not expressing FLP (top
840 panels; strain BN793) or expressing FLP in the hypodermis either without (middle
841 panels; *dpy-7p::FLP* driver; strain BN1121) or with GFPdeg in the hypodermis
842 (bottom panels; *dpy-7p::FLP* driver; strain BN1122). A single focal plane of the
843 hypodermis is shown. Scale bar 10 µm. (B) Quantification of GFP::MEL-28 at the
844 nuclear envelope of hypodermal nuclei. Each point represents a single nucleus. Data
845 were acquired from at least 10 animals in two independent experiments; *n* for each
846 genotype is indicated in parentheses. P values from Kruskal-Wallis rank sum tests
847 and adjusted with Dunn's test for multiple comparisons (Benjamini & Hochberg
848 method) are indicated.

849 Figure 4. Degradation of GFP::MEL-28 in intestinal cells. (A) Schematic
850 representation of the GFPdeg strategy. The vhhGFP4::ZIF-1 fusion protein targets
851 GFP-tagged proteins for rapid degradation. Temporal and spatial control is provided
852 by the *hsp-16.41* promoter and tissue-specific FLP expression, respectively. (B)
853 Quantification of GFP::MEL-28 at the nuclear envelope of hypodermal nuclei of
854 young adults either without the GFPdeg system (Control; strain BN452) or with the
855 GFPdeg system but without induction (GFPdeg; strain BN1084). P value from t test
856 is indicated. (C) Quantification of GFP::MEL-28 at the nuclear envelope of anterior
857 intestinal nuclei of young adults after 1 or 2 rounds of GFPdeg induction in the
858 intestine (*nhx-2p::FLP* driver; strain BN1118). Control (strain BN452) and constitutive
859 degradation (*elt-2p::vhhGFP4::zif-1*; strain BN746) are included for comparison.
860 Graph details are explained in Figure 3. P values from pair-wise t tests and adjusted
861 for multiple comparisons (Benjamini & Hochberg method) are indicated. (D) Confocal
862 micrographs of *gfp::mel-28* young adults without GFPdeg (top panels; strain BN452),
863 inducible intestinal GFPdeg (middle panels; strain BN1118) or constitutive intestinal
864 GFPdeg (bottom panels; strain BN746). A single focal plane of the anterior pair of
865 intestinal nuclei is shown. Scale bar 10 µm.

866 Figure 5. Kinetics of GFP::MEL-28 degradation in hypodermal cells. (A) Confocal
867 micrographs of *gfp::mel-28* young adults either without induction or 1-24 h after
868 induction of GFPdeg in the hypodermis (*dpy-7p::FLP* driver; strain BN1084). A single
869 focal plane of the hypodermis is shown. Scale bar 10 µm. (B) Quantification of
870 GFP::MEL-28 at the nuclear envelope of hypodermal nuclei. Graph details are
871 explained in Figure 3.

872 Figure 6. Efficient protein depletion by combined gene KO and GFPdeg. (A)
873 Schematic representation of the combined KO and GFPdeg strategy. A single FLP
874 driver controls in a tissue-specific manner both KO (left) and protein degradation
875 (right) of a gene tagged with the GFP KO cassette. (B) Confocal micrographs of
876 *g>f>p::npp-2* L4 larvae either not expressing FLP (left panel; strain BN1082),
877 expressing FLP in the hypodermis (middle panel; *dpy-7p::FLP* driver; strain BN1111)
878 or expressing FLP and vhhGFP4::ZIF-1 in the hypodermis (right panel; *dpy-7p::FLP*
879 driver; strain BN1086). A single focal plane of the hypodermis is shown. Scale bar 10
880 µm. (C) Quantification of GFP::NPP-2 at the nuclear envelope of hypodermal nuclei.
881 Graph details are explained in Figure 3. (D) Survival curves for animals expressing
882 GFP::NPP-2 alone (blue; strain BN1082) or combined with either FLP in the

883 hypodermis (dark red; strain BN1111) or FLP and GFPdeg in the hypodermis (red;
884 strain BN1086). A strain with hypodermal FLP and GFPdeg but without target was
885 included as control (green; BN1097). The lifespan of the two strains with depletion of
886 GFP::NPP-2 in the hypodermis was significantly shorter compared to the two control
887 strains (*** indicates p<1e-08). More than 175 animals were analysed for each
888 genotype.

889 Figure 7. Tissue-specific identification of transcribed genes by RAPID. (A) Schematic
890 representation of the RAPID method. Spatial control is provided by tissue-specific
891 FLP expression that leads to excision of the *mCherry::his-58* cassette and basal
892 transcription of *Dam::rpb-6* from the *hsp-16.41* promoter. Dam::RPB-6 incorporates
893 into RNA polymerases and marks GATC sites in transcribed genes. A *GFP::Dam*
894 transgene is used in parallel to control for differences in chromatin accessibility and
895 unspecific methylation (not shown). (B-E) Data based on two replicas of L4s
896 expressing either Dam::RPB-6 (strain BN1414) or GFP::Dam (strain BN561) in the
897 hypodermis. The analysis was restricted to 19,975 protein coding genes annotated in
898 WBCel235. (B) RAPID signal (blue) averaged in 10 bp bins across all genes (left
899 graph) or across 2331 expressed genes (right graph) from 2 kb upstream of the
900 transcriptional start site (TSS) to 2 kb downstream of the transcriptional end site
901 (TES). The signal from TSS to TES was extrapolated to an arbitrary length of 3 kb
902 for each gene. The distribution of the active chromatin mark H3K36me3 (BANNISTER
903 *et al.* 2005) is included for comparison. The heatmap (middle graph) represents the
904 individual genes from the left graph. (C) Representation of Dam::RPB-6/GFP::Dam
905 ratios for individual replicas (Rep 1, Rep 2) at selected loci. Genes with significant
906 RAPID signal are indicated (FDR<0.05). (D-E) Comparison of the 2331 transcribed
907 genes identified by RAPID with three alternative methods for transcriptomic profiling
908 (see main text for details). Numbers in parentheses indicate the number of protein
909 coding genes reported in each study.

910

911 Supplementary Figure S1. Characterization of novel FLP drivers. Upon temperature
912 induction of the *hsp-16.41* promoter, the reporter expresses red (mCh) or green
913 (GFP) histone HIS-58 in cell lineages without or with FLP-mediated recombination,
914 respectively. (A) Recombination activity by *lin-31p::FLP::SL2::mNG* is observed in
915 the head (left panel) and central region (right panel) of BN1023 animals. Bright
916 GFP::HIS-58 expression is observed in the nuclei of cells forming the vulva (filled
917 arrows), whereas faint expression is detected in the hypodermis (open arrows; right
918 panel). Presumably, the faint expression is derived from Pn.p cells that fuse with
919 hyp7. (B) Recombination activity by *gpa-14p::FLP::SL2::mNG* is observed in the
920 head (left panel) and tail (right panel) of BN1208 animals. Filled arrows point to
921 nuclei expressing GFP::HIS-58 but not mCh::HIS-58 (i.e. recombination of both
922 alleles); a double arrow points to a nucleus expressing both fluorescent proteins (i.e.
923 recombination of one allele) and open arrows indicate cells that express diffuse mNG
924 (and hence also FLP) but not GFP::HIS-58. (C) Expression of mNG from the *unc-*
925 *17p::FLP::SL2::mNG* transgene overlaps with mKate2 signal from endogenously
926 tagged *unc-17* (lower left panel) and recombination (GFP::HIS-58) is detected as
927 expected in multiple neurons in the head (upper left panel) and ventral nerve cord
928 (upper right panel) of BN1133 animals. Unexpectedly, GFP::HIS-58 is also observed
929 in hypodermal nuclei (lower right panel). (D) Recombination activity by *hlh-*
930 *12p::FLP::SL2::mTagBFP2* is observed in the distal tip cell of BN1319 animals. The
931 distal tip cell is marked by co-expressed mTagBFP2. Scale bars 10 µm.

Supplementary Figure S2. Overlap between protein coding gene sets identified by TaDa in seam cells and hypodermis (KATSANOS *et al.* 2021) and by RAPID in hypodermis (this study).

References

Altun, Z. F., and D. H. Hall, 2009 Coelomocyte system, pp. in *WormAtlas*.

Armenti, S. T., L. L. Lohmer, D. R. Sherwood and J. Nance, 2014 Repurposing an endogenous degradation system for rapid and targeted depletion of C. elegans proteins. Development 141**:** 4640-4647.

Arribere, J. A., H. Kuroyanagi and H. A. Hundley, 2020 mRNA Editing, Processing and Quality Control in Caenorhabditis elegans. Genetics 215**:** 531-568.

Askjaer, P., and J. C. Harr, 2021 Genetic approaches to revealing the principles of nuclear architecture. Curr Opin Genet Dev 67**:** 52-60.

Ayuso, C., and P. Askjaer, 2019 Spatiotemporal control of genome recombination through combined FLP-Frt and GAL4-UAS technologies. MicroPubl Biol 2019.

Bannister, A. J., R. Schneider, F. A. Myers, A. W. Thorne, C. Crane-Robinson *et al.*, 2005 Spatial distribution of di- and tri-methyl lysine 36 of histone H3 at active genes. J Biol Chem 280**:** 17732-17736.

Bardou, P., J. Mariette, F. Escudie, C. Djemiel and C. Klopp, 2014 jvenn: an interactive Venn diagram viewer. BMC Bioinformatics 15**:** 293.

Bhoi, A., F. Palladino and P. Fabrizio, 2021 Auxin confers protection against ER stress in Caenorhabditis elegans. Biol Open 10.

Blazie, S. M., H. C. Geissel, H. Wilky, R. Joshi, J. Newbern *et al.*, 2017 Alternative Polyadenylation Directs Tissue-Specific miRNA Targeting in Caenorhabditis elegans Somatic Tissues. Genetics 206**:** 757-774.

Cabianca, D. S., C. Munoz-Jimenez, V. Kalck, D. Gaidatzis, J. Padeken *et al.*, 2019 Active chromatin marks drive spatial sequestration of heterochromatin in C. elegans nuclei. Nature 569**:** 734-739.

Caussinus, E., O. Kanca and M. Affolter, 2011 Fluorescent fusion protein knockout mediated by anti-GFP nanobody. Nat Struct Mol Biol 19**:** 117-121.

Cohen, S., L. Kramarski, S. Levi, N. Deshe, O. Ben David *et al.*, 2019 Nonsense mutation-dependent reinitiation of translation in mammalian cells. Nucleic Acids Res 47**:** 6330-6338.

Davis, L., I. Radman, A. Goutou, A. Tynan, K. Baxter *et al.*, 2021 Precise optical control of gene expression in C elegans using improved genetic code expansion and Cre recombinase. Elife 10.

Davis, M. W., J. J. Morton, D. Carroll and E. M. Jorgensen, 2008 Gene activation using FLP recombinase in C. elegans. PLoS Genet 4**:** e1000028.

de la Cruz Ruiz, P., R. Romero-Bueno and P. Askjaer, 2022 Analysis of Nuclear Pore Complexes in Caenorhabditis elegans by Live Imaging and Functional Genomics. Methods Mol Biol 2502**:** 161-182.

Dobrzynska, A., P. Askjaer and Y. Gruenbaum, 2016 Lamin-Binding Proteins in Caenorhabditis elegans. Methods Enzymol 569**:** 455-483.

Driesschaert, B., L. Mergan and L. Temmerman, 2021 Conditional gene expression in invertebrate animal models. J Genet Genomics 48**:** 14-31.

Fernandez, A. G., and F. Piano, 2006 MEL-28 is downstream of the Ran cycle and is required for nuclear-envelope function and chromatin maintenance. Curr Biol 16**:** 1757-1763.

Friedland, A. E., Y. B. Tzur, K. M. Esvelt, M. P. Colaiacovo, G. M. Church *et al.*, 2013 Heritable genome editing in C. elegans via a CRISPR-Cas9 system. Nat Methods 10**:** 741-743.

Frokjaer-Jensen, C., M. W. Davis, M. Ailion and E. M. Jorgensen, 2012 Improved Mos1-mediated transgenesis in C. elegans. Nat Methods 9**:** 117-118.

Frokjaer-Jensen, C., M. W. Davis, C. E. Hopkins, B. J. Newman, J. M. Thummel *et al.*, 2008 Single-copy insertion of transgenes in Caenorhabditis elegans. Nat Genet 40**:** 1375-1383.

Frokjaer-Jensen, C., M. W. Davis, M. Sarov, J. Taylor, S. Flibotte *et al.*, 2014 Random and targeted transgene insertion in Caenorhabditis elegans using a modified Mos1 transposon. Nat Methods 11**:** 529-534.

Galy, V., P. Askjaer, C. Franz, C. Lopez-Iglesias and I. W. Mattaj, 2006 MEL-28, a novel nuclear-envelope and kinetochore protein essential for zygotic nuclear-envelope assembly in C. elegans. Curr Biol 16**:** 1748-1756.

Ge, M. H., W. Wang, T. H. Wu, X. Wen, U. Al-Sheikh *et al.*, 2020 Dual Recombining-out System for Spatiotemporal Gene Expression in C. elegans. iScience 23**:** 101567.

Gomez-Saldivar, G., A. Fernandez, Y. Hirano, M. Mauro, A. Lai *et al.*, 2016 Identification of Conserved MEL-28/ELYS Domains with Essential Roles in Nuclear Assembly and Chromosome Segregation. PLoS Genet 12**:** e1006131.

Gomez-Saldivar, G., J. Osuna-Luque, J. I. Semple, D. A. Glauser, S. Jarriault *et al.*, 2020 Tissue-Specific Transcription Footprinting Using RNA Pol DamID (RAPID) in Caenorhabditis elegans. Genetics.

Gorjanacz, M., E. P. Klerkx, V. Galy, R. Santarella, C. Lopez-Iglesias *et al.*, 2007 Caenorhabditis elegans BAF-1 and its kinase VRK-1 participate directly in post-mitotic nuclear envelope assembly. EMBO J 26**:** 132-143.

Haenni, S., Z. Ji, M. Hoque, N. Rust, H. Sharpe *et al.*, 2012 Analysis of C. elegans intestinal gene expression and polyadenylation by fluorescence-activated nuclei sorting and 3'-end-seq. Nucleic Acids Res 40**:** 6304-6318.

Harr, J. C., C. D. Schmid, C. Munoz-Jimenez, R. Romero-Bueno, V. Kalck *et al.*, 2020 Loss of an H3K9me anchor rescues laminopathy-linked changes in nuclear organization and muscle function in an Emery-Dreifuss muscular dystrophy model. Genes Dev.

Hills-Muckey, K., M. A. Q. Martinez, N. Stec, S. Hebbar, J. Saldanha *et al.*, 2021 An engineered, orthogonal auxin analog/AtTIR1(F79G) pairing improves both specificity and efficacy of the auxin degradation system in Caenorhabditis elegans. Genetics.

Hubbard, E. J., 2014 FLP/FRT and Cre/lox recombination technology in C. elegans. Methods 68**:** 417-424.

Hubbard, E. J., and D. Greenstein, 2005 Introduction to the germ line. WormBook**:** 1-4.

Kage-Nakadai, E., R. Imae, Y. Suehiro, S. Yoshina, S. Hori *et al.*, 2014 A conditional knockout toolkit for Caenorhabditis elegans based on the Cre/loxP recombination. PLoS One 9**:** e114680.

Kaletsky, R., V. Yao, A. Williams, A. M. Runnels, A. Tadych *et al.*, 2018 Transcriptome analysis of adult Caenorhabditis elegans cells reveals tissue-specific gene and isoform expression. PLoS Genet 14**:** e1007559.

Kassambara, A., 2020 ggpubr: 'ggplot2' Based Publication Ready Plots, pp.

1029 Katsanos, D., M. Ferrando-Marco, I. Razzaq, G. Aughey, T. D. Southall *et al.*, 2021
1030 Gene expression profiling of epidermal cell types in C. elegans using
1031 Targeted DamID. Development 148.
1032 Kimble, J., and H. Seidel, 2008 C. elegans germline stem cells and their niche in
1033 *StemBook*, Cambridge (MA).
1034 Konietzka, J., M. Fritz, S. Spiri, R. McWhirter, A. Leha *et al.*, 2020 Epidermal Growth
1035 Factor Signaling Promotes Sleep through a Combined Series and Parallel
1036 Neural Circuit. Curr Biol 30**:** 1-16 e13.
1037 Kroetz, M. B., and D. Zarkower, 2015 Cell-Specific mRNA Profiling of the
1038 Caenorhabditis elegans Somatic Gonadal Precursor Cells Identifies Suites of
1039 Sex-Biased and Gonad-Enriched Transcripts. G3 (Bethesda) 5**:** 2831-2841.
1040 Loria, P. M., J. Hodgkin and O. Hobert, 2004 A conserved postsynaptic
1041 transmembrane protein affecting neuromuscular signaling in Caenorhabditis
1042 elegans. J Neurosci 24**:** 2191-2201.
1043 Ma, X., G. Zhan, M. C. Sleumer, S. Chen, W. Liu *et al.*, 2016 Analysis of C. elegans
1044 muscle transcriptome using trans-splicing-based RNA tagging (SRT). Nucleic
1045 Acids Res 44**:** e156.
1046 Macias-Leon, J., and P. Askjaer, 2018 Efficient FLP-mediated germ-line
1047 recombination in C. elegans. MicroPubl Biol 2018.
1048 Marshall, O. J., and A. H. Brand, 2015 damidseq_pipeline: an automated pipeline for
1049 processing DamID sequencing datasets. Bioinformatics 31**:** 3371-3373.
1050 Marshall, O. J., T. D. Southall, S. W. Cheetham and A. H. Brand, 2016 Cell-type-
1051 specific profiling of protein-DNA interactions without cell isolation using
1052 targeted DamID with next-generation sequencing. Nat Protoc 11**:** 1586-1598.
1053 McGhee, J. D., 2007 The C. elegans intestine. WormBook**:** 1-36.
1054 Monsalve, G. C., K. R. Yamamoto and J. D. Ward, 2019 A New Tool for Inducible
1055 Gene Expression in Caenorhabditis elegans. Genetics 211**:** 419-430.
1056 Munoz-Jimenez, C., C. Ayuso, A. Dobrzynska, A. Torres-Mendez, P. C. Ruiz *et al.*,
1057 2017 An Efficient FLP-Based Toolkit for Spatiotemporal Control of Gene
1058 Expression in Caenorhabditis elegans. Genetics 206**:** 1763-1778.
1059 Nance, J., and C. Frokjaer-Jensen, 2019 The Caenorhabditis elegans Transgenic
1060 Toolbox. Genetics 212**:** 959-990.
1061 Nehrke, K., and J. E. Melvin, 2002 The NHX family of Na+-H+ exchangers in
1062 Caenorhabditis elegans. J Biol Chem 277**:** 29036-29044.
1063 Nonet, M. L., 2020 Efficient Transgenesis in Caenorhabditis elegans Using Flp
1064 Recombinase-Mediated Cassette Exchange. Genetics 215**:** 903-921.
1065 Packer, J. S., Q. Zhu, C. Huynh, P. Sivaramakrishnan, E. Preston *et al.*, 2019 A
1066 lineage-resolved molecular atlas of C. elegans embryogenesis at single-cell
1067 resolution. Science.
1068 Pereira, L., P. Kratsios, E. Serrano-Saiz, H. Sheftel, A. E. Mayo *et al.*, 2015 A
1069 cellular and regulatory map of the cholinergic nervous system of C. elegans.
1070 Elife 4.
1071 Porta-de-la-Riva, M., A. C. Gonzalez, N. Sanfeliu-Cerdán, S. Karimi, S. González-
1072 Bolívar *et al.*, 2021 Deploying photons for communication within neuronal
1073 networks. bioRxiv**:** 2021.2008.2002.454613.
1074 Reece-Hoyes, J. S., J. Shingles, D. Dupuy, C. A. Grove, A. J. Walhout *et al.*, 2007
1075 Insight into transcription factor gene duplication from Caenorhabditis elegans
1076 Promoterome-driven expression patterns. BMC Genomics 8**:** 27.
1077 Rodenas, E., C. Gonzalez-Aguilera, C. Ayuso and P. Askjaer, 2012 Dissection of the
1078 NUP107 nuclear pore subcomplex reveals a novel interaction with spindle

1079 assembly checkpoint protein MAD1 in Caenorhabditis elegans. Mol Biol Cell
1080 23: 930-944.
1081 Ruijtenberg, S., and S. van den Heuvel, 2015 G1/S Inhibitors and the SWI/SNF
1082 Complex Control Cell-Cycle Exit during Muscle Differentiation. Cell 162: 300-
1083 313.
1084 Sauer, B., 1987 Functional expression of the cre-lox site-specific recombination
1085 system in the yeast Saccharomyces cerevisiae. Mol Cell Biol 7: 2087-2096.
1086 Savas, J. N., B. H. Toyama, T. Xu, J. R. Yates, 3rd and M. W. Hetzer, 2012
1087 Extremely long-lived nuclear pore proteins in the rat brain. Science 335: 942.
1088 Schindelin, J., I. Arganda-Carreras, E. Frise, V. Kaynig, M. Longair *et al.*, 2012 Fiji:
1089 an open-source platform for biological-image analysis. Nat Methods 9: 676-
1090 682.
1091 Schmitt, C., C. Schultheis, N. Pokala, S. J. Husson, J. F. Liewald *et al.*, 2012
1092 Specific expression of channelrhodopsin-2 in single neurons of
1093 Caenorhabditis elegans. PLoS One 7: e43164.
1094 Schwartz, M. L., and E. M. Jorgensen, 2016 SapTrap, a Toolkit for High-Throughput
1095 CRISPR/Cas9 Gene Modification in Caenorhabditis elegans. Genetics 202:
1096 1277-1288.
1097 Senecoff, J. F., R. C. Bruckner and M. M. Cox, 1985 The FLP recombinase of the
1098 yeast 2-micron plasmid: characterization of its recombination site. Proc Natl
1099 Acad Sci U S A 82: 7270-7274.
1100 Sharma, R., D. Ritler and P. Meister, 2016 Tools for DNA adenine methyltransferase
1101 identification analysis of nuclear organization during C. elegans development.
1102 Genesis 54: 151-159.
1103 Southall, T. D., K. S. Gold, B. Egger, C. M. Davidson, E. E. Caygill *et al.*, 2013 Cell-
1104 type-specific profiling of gene expression and chromatin binding without cell
1105 isolation: assaying RNA Pol II occupancy in neural stem cells. Dev Cell 26:
1106 101-112.
1107 Steiner, F. A., P. B. Talbert, S. Kasinathan, R. B. Deal and S. Henikoff, 2012 Cell-
1108 type-specific nuclei purification from whole animals for genome-wide
1109 expression and chromatin profiling. Genome Res 22: 766-777.
1110 Stempor, P., and J. Ahringer, 2016 SeqPlots - Interactive software for exploratory
1111 data analyses, pattern discovery and visualization in genomics. Wellcome
1112 Open Res 1: 14.
1113 Stiernagle, T., 2006 Maintenance of C. elegans. WormBook: 1-11.
1114 Tamai, K. K., and K. Nishiwaki, 2007 bHLH transcription factors regulate organ
1115 morphogenesis via activation of an ADAMTS protease in C. elegans. Dev Biol
1116 308: 562-571.
1117 Tan, P. B., M. R. Lackner and S. K. Kim, 1998 MAP kinase signaling specificity
1118 mediated by the LIN-1 Ets/LIN-31 WH transcription factor complex during C.
1119 elegans vulval induction. Cell 93: 569-580.
1120 Team, R., 2020a RStudio: Integrated Development Environment for R, pp. RStudio,
1121 PBC.
1122 Team, R. C., 2020b R: A Language and Environment for Statistical Computing, pp. R
1123 Foundation for Statistical Computing.
1124 Therneau, T., 2020 A Package for Survival Analysis in R, pp.
1125 Thorvaldsdottir, H., J. T. Robinson and J. P. Mesirov, 2013 Integrative Genomics
1126 Viewer (IGV): high-performance genomics data visualization and exploration.
1127 Brief Bioinform 14: 178-192.

Toyama, B. H., J. N. Savas, S. K. Park, M. S. Harris, N. T. Ingolia *et al.*, 2013 Identification of long-lived proteins reveals exceptional stability of essential cellular structures. Cell 154**:** 971-982.

Van de Walle, P., C. Munoz-Jimenez, P. Askjaer, L. Schoofs and L. Temmerman, 2020 DamID identifies targets of CEH-60/PBX that are associated with neuron development and muscle structure in Caenorhabditis elegans. PLoS One 15**:** e0242939.

Voutev, R., and E. J. Hubbard, 2008 A "FLP-Out" system for controlled gene expression in Caenorhabditis elegans. Genetics 180**:** 103-119.

Wang, S., N. H. Tang, P. Lara-Gonzalez, Z. Zhao, D. K. Cheerambathur *et al.*, 2017 A toolkit for GFP-mediated tissue-specific protein degradation in C. elegans. Development 144**:** 2694-2701.

Watts, J. S., H. F. Harrison, S. Omi, Q. Guenthers, J. Dalelio *et al.*, 2020 New Strains for Tissue-Specific RNAi Studies in Caenorhabditis elegans. G3 (Bethesda) 10**:** 4167-4176.

Wickham, H., 2016 *ggplot2: Elegant Graphics for Data Analysis*. Springer-Verlag New York.

Widmer, Y. F., A. Bilican, R. Bruggmann and S. G. Sprecher, 2018 Regulators of Long-Term Memory Revealed by Mushroom Body-Specific Gene Expression Profiling in Drosophila melanogaster. Genetics 209**:** 1167-1181.

Wurmthaler, L. A., M. Sack, K. Gense, J. S. Hartig and M. Gamerdinger, 2019 A tetracycline-dependent ribozyme switch allows conditional induction of gene expression in Caenorhabditis elegans. Nat Commun 10**:** 491.

Zhang, L., J. D. Ward, Z. Cheng and A. F. Dernburg, 2015 The auxin-inducible degradation (AID) system enables versatile conditional protein depletion in C. elegans. Development 142**:** 4374-4384.

Figure 1

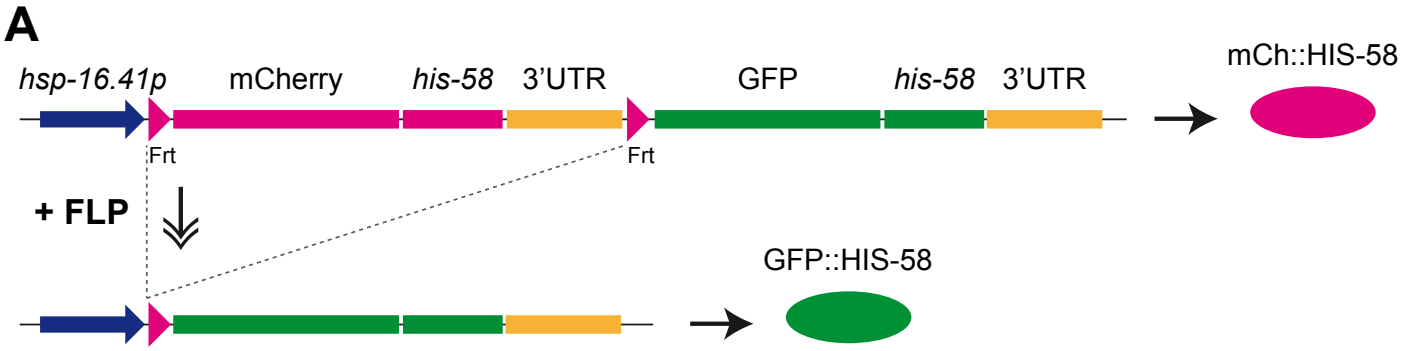

B

a' ckb-3p::FLP::SL2::mNG
Z1
Z4

a'' ckb-3p::FLP::SL2::mNG

b' hlh-12p::FLP::SL2::mNG
DTC

b'' hlh-12p::FLP::SL2::mNG
DTC

c' lin-31p::FLP::SL2::mNG
P1.p
P2.p
P3.p
P4.p
P5.p
P6.p
P7.p

c'' lin-31p::FLP::SL2::mNG
P1.p
P2.p
P3.p
P4.p
vulA-F

d' nhx-2p::FLP::SL2::mNG

d'' nhx-2p::FLP::SL2::mNG

e' unc-122p::FLP::SL2::mNG
ccPR+ccAR
ccPL+ccAL

e'' unc-122p::FLP::SL2::mNG
ccDL
ccDR

Figure 2

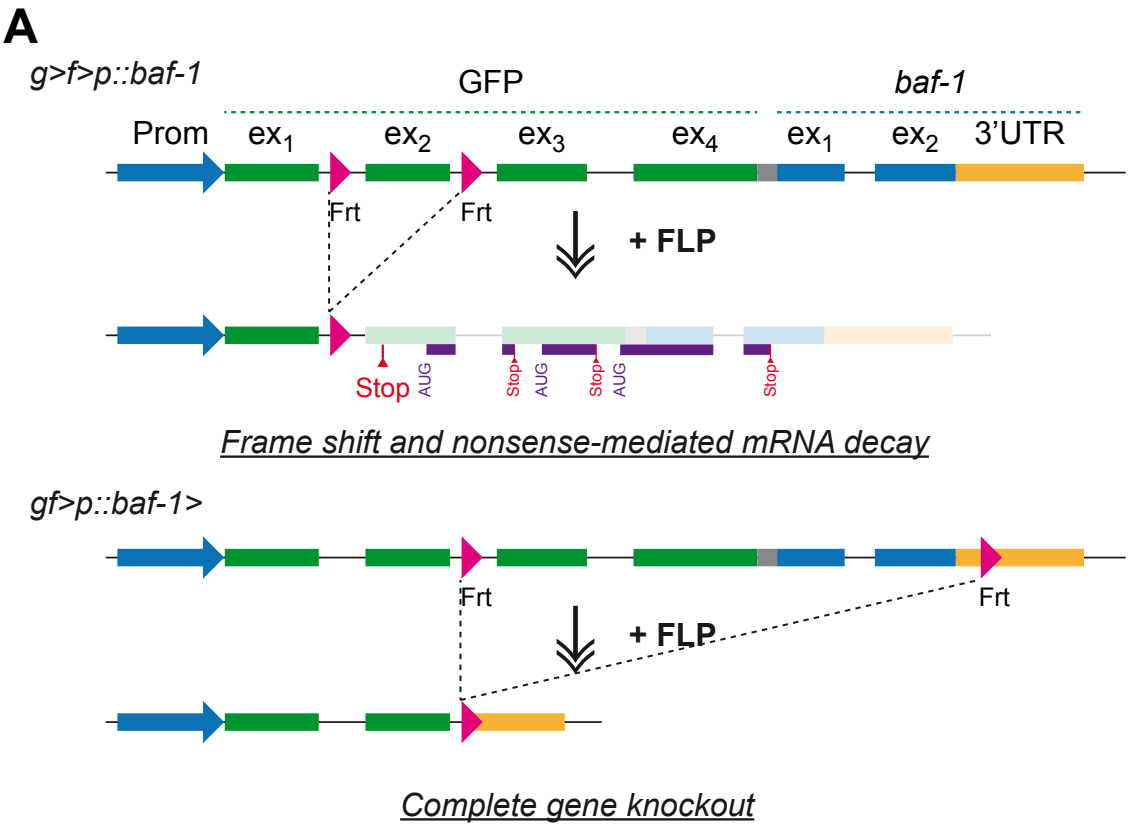
A
g>f>p::baf-1
GFP
baf-1
Prom
ex1
ex2
ex3
ex4
ex1
ex2
3'UTR
Frt
Frt
+ FLP
Stop
AUG
Stop
AUG
Stop
AUG
Stop
Frame shift and nonsense-mediated mRNA decay
gf>p::baf-1>
Frt
Frt
+ FLP
Complete gene knockout

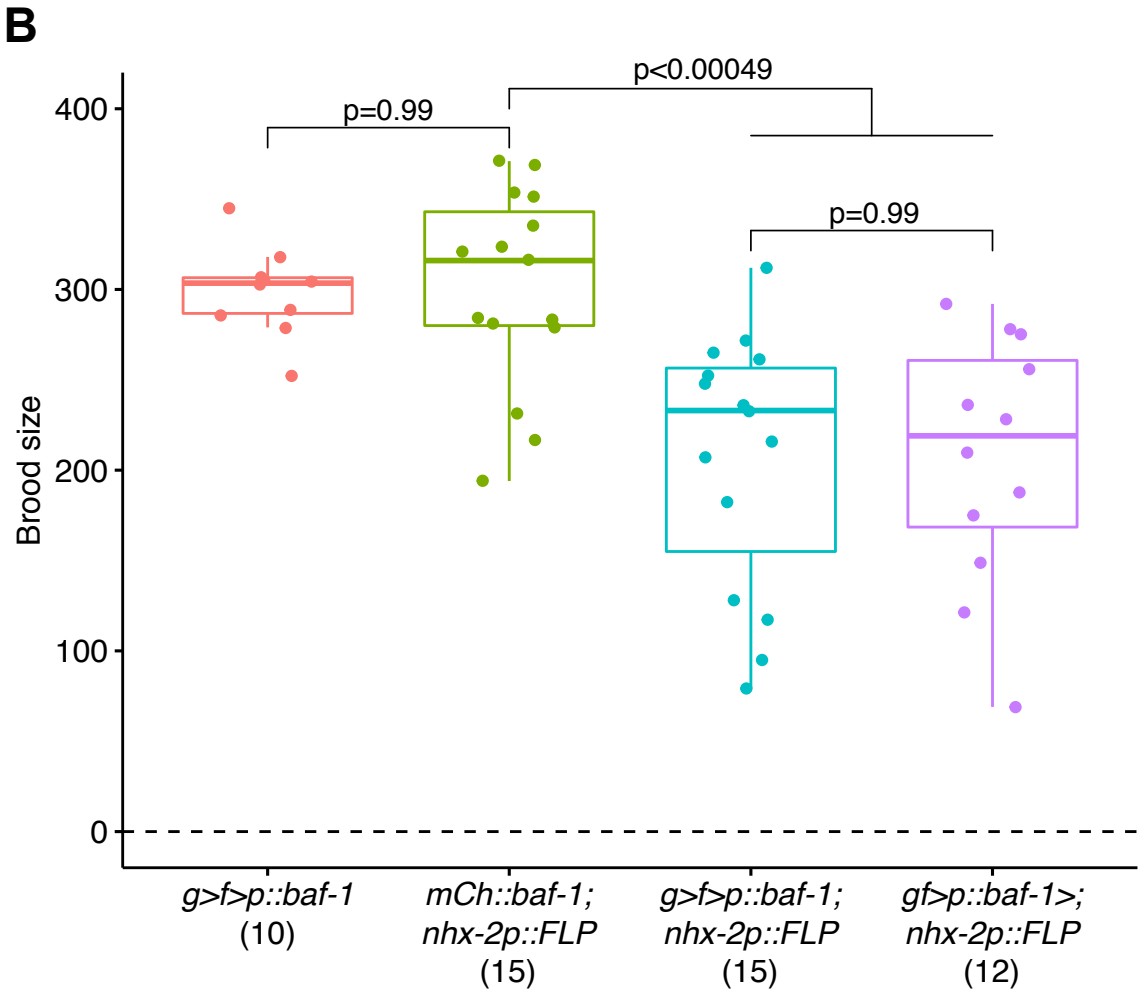
B
p<0.00049
p=0.99
p=0.99
Brood size
400
300
200
100
0
g>f>p::baf-1
(10)
mCh::baf-1;
nhx-2p::FLP
(15)
g>f>p::baf-1;
nhx-2p::FLP
(15)
gf>p::baf-1>;
nhx-2p::FLP
(12)

Figure 3

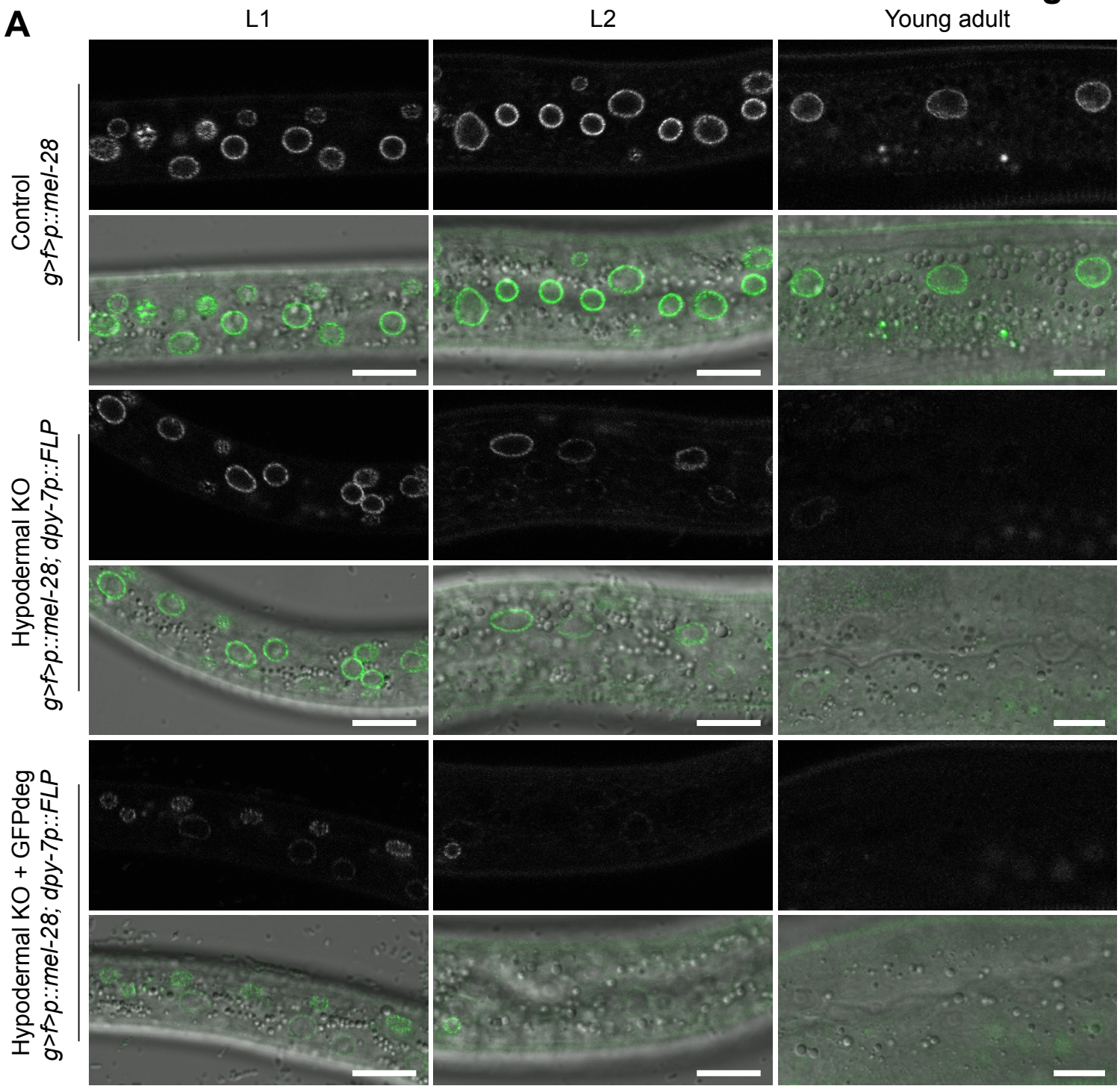
A
L1
L2
Young adult
Control
g>f>p::mel-28
Hypodermal KO
g>f>p::mel-28; dpy-7p::FLP
Hypodermal KO + GFPdeg
g>f>p::mel-28; dpy-7p::FLP

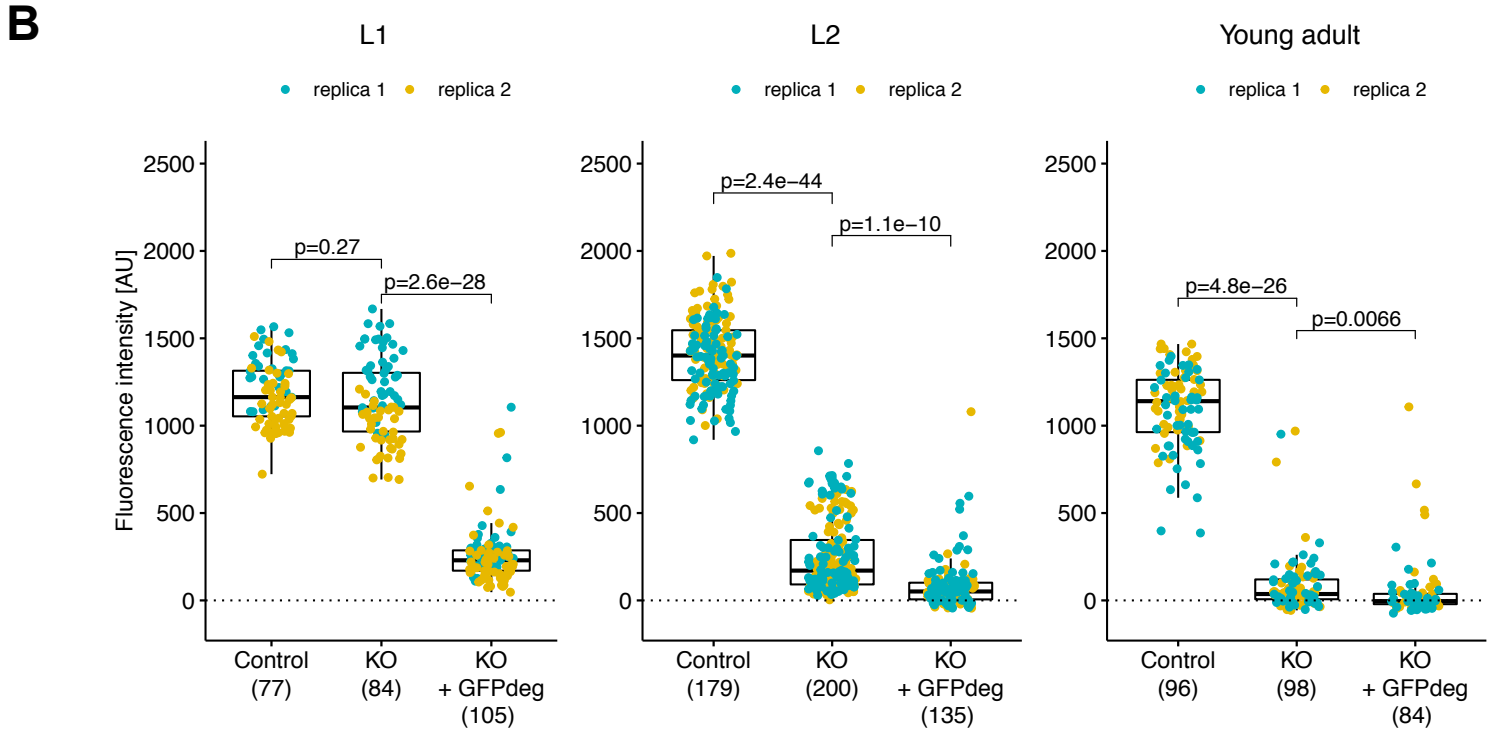
B
L1
L2
Young adult
replica 1
replica 2
Fluorescence intensity [AU]
2500
2000
1500
1000
500
0
p=0.27
p=2.6e−28
p=2.4e−44
p=1.1e−10
p=4.8e−26
p=0.0066
Control (77)
KO (84)
KO + GFPdeg (105)
Control (179)
KO (200)
KO + GFPdeg (135)
Control (96)
KO (98)
KO + GFPdeg (84)

Figure 4

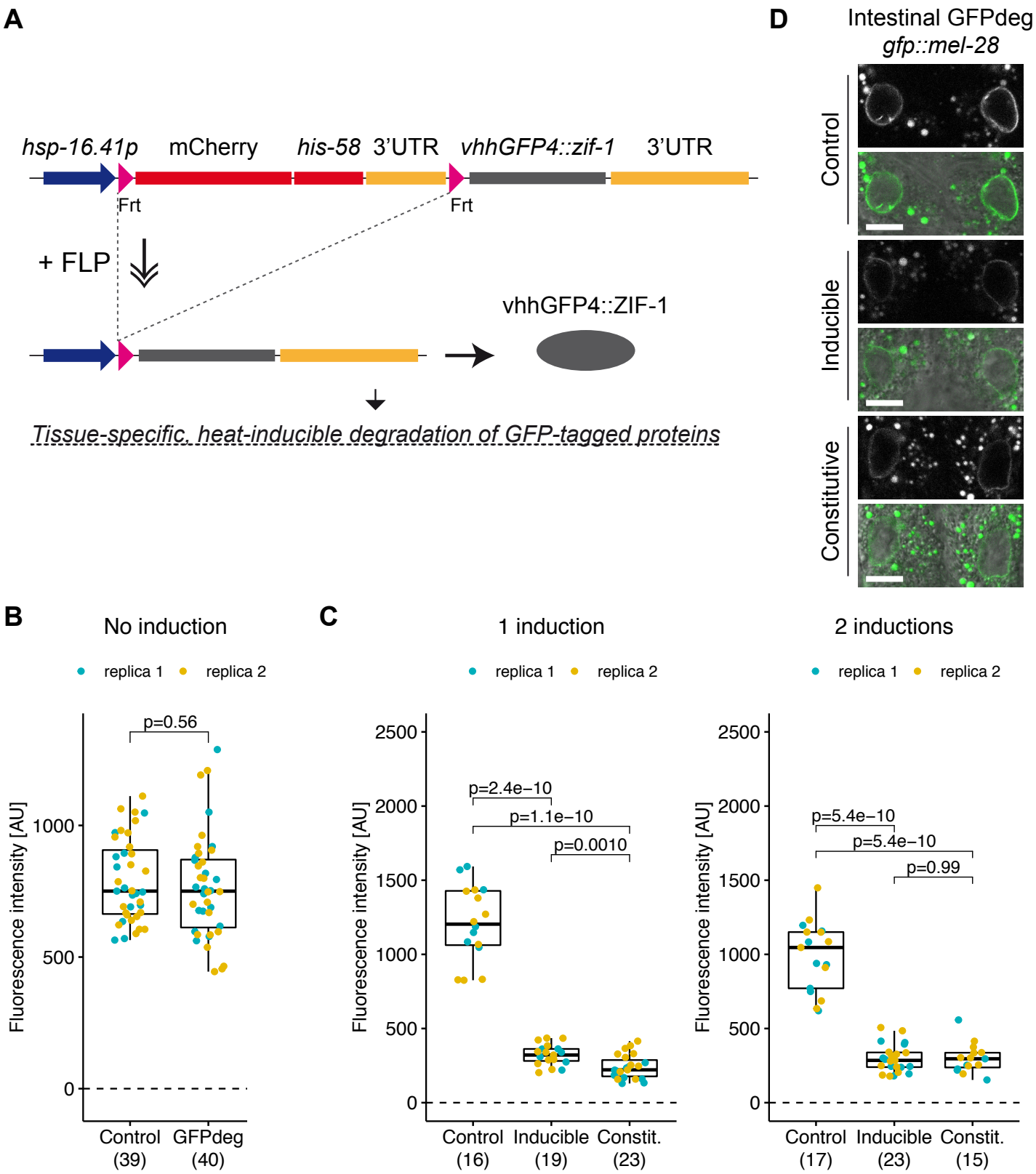
A
hsp-16.41p
mCherry
his-58 3'UTR
vhhGFP4::zif-1
3'UTR
Frt
Frt
+ FLP
vhhGFP4::ZIF-1
Tissue-specific, heat-inducible degradation of GFP-tagged proteins
D
Intestinal GFPdeg
gfp::mel-28
Control
Inducible
Constitutive
B
No induction
replica 1
replica 2
p=0.56
Fluorescence intensity [AU]
Control (39)
GFPdeg (40)
C
1 induction
p=2.4e−10
p=1.1e−10
p=0.0010
Control (16)
Inducible (19)
Constit. (23)
2 inductions
p=5.4e−10
p=5.4e−10
p=0.99
Control (17)
Inducible (23)
Constit. (15)

Figure 5

A

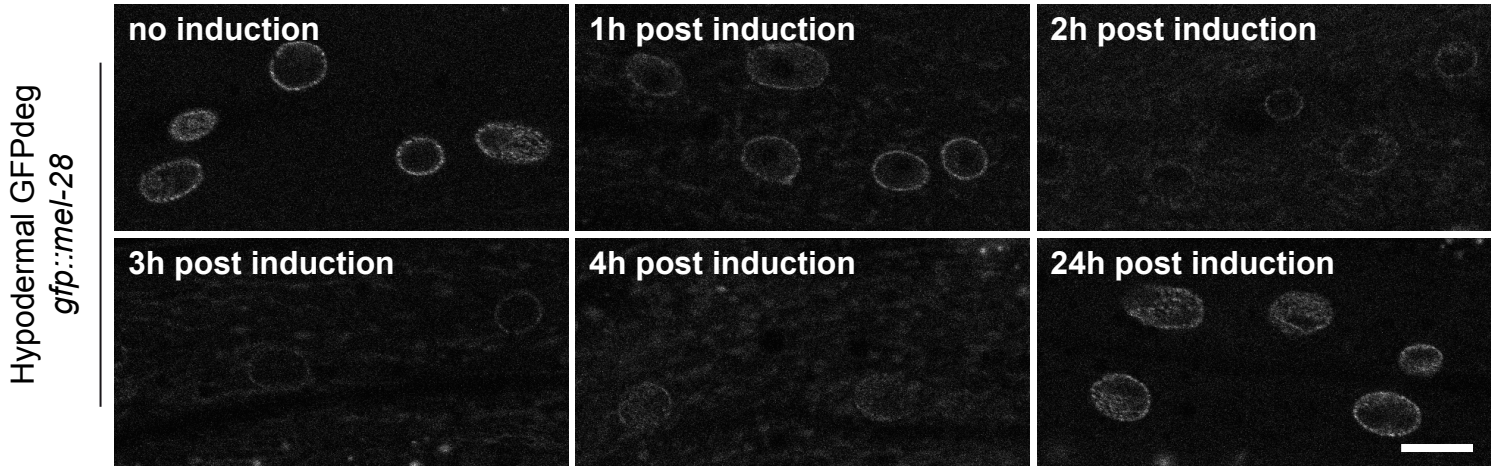
Hypodermal GFPdeg
gfp::mel-28
no induction
1h post induction
2h post induction
3h post induction
4h post induction
24h post induction

B

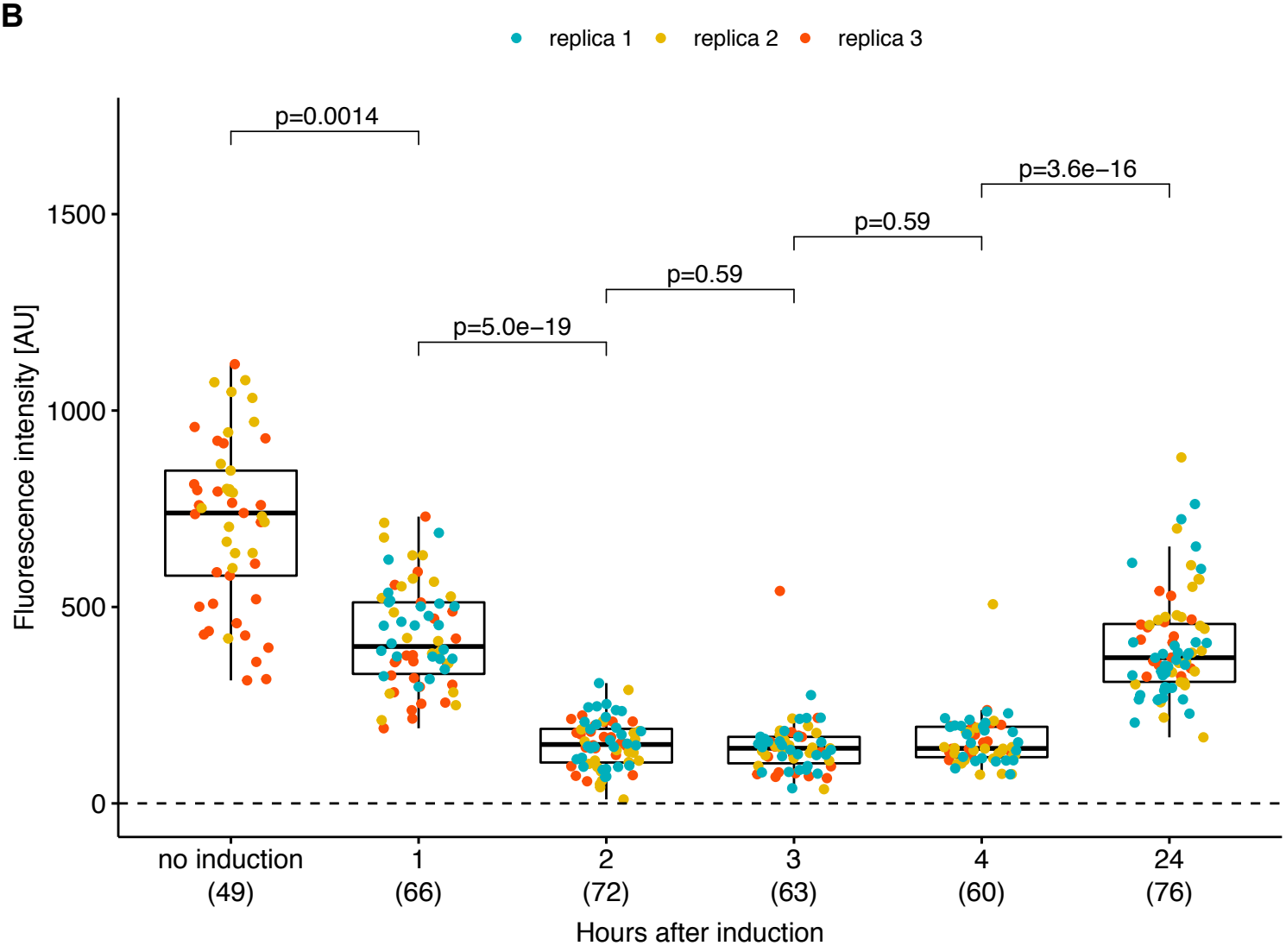
replica 1
replica 2
replica 3
p=0.0014
p=5.0e−19
p=0.59
p=0.59
p=3.6e−16
Fluorescence intensity [AU]
0
500
1000
1500
no induction (49)
1 (66)
2 (72)
3 (63)
4 (60)
24 (76)
Hours after induction

Figure 6

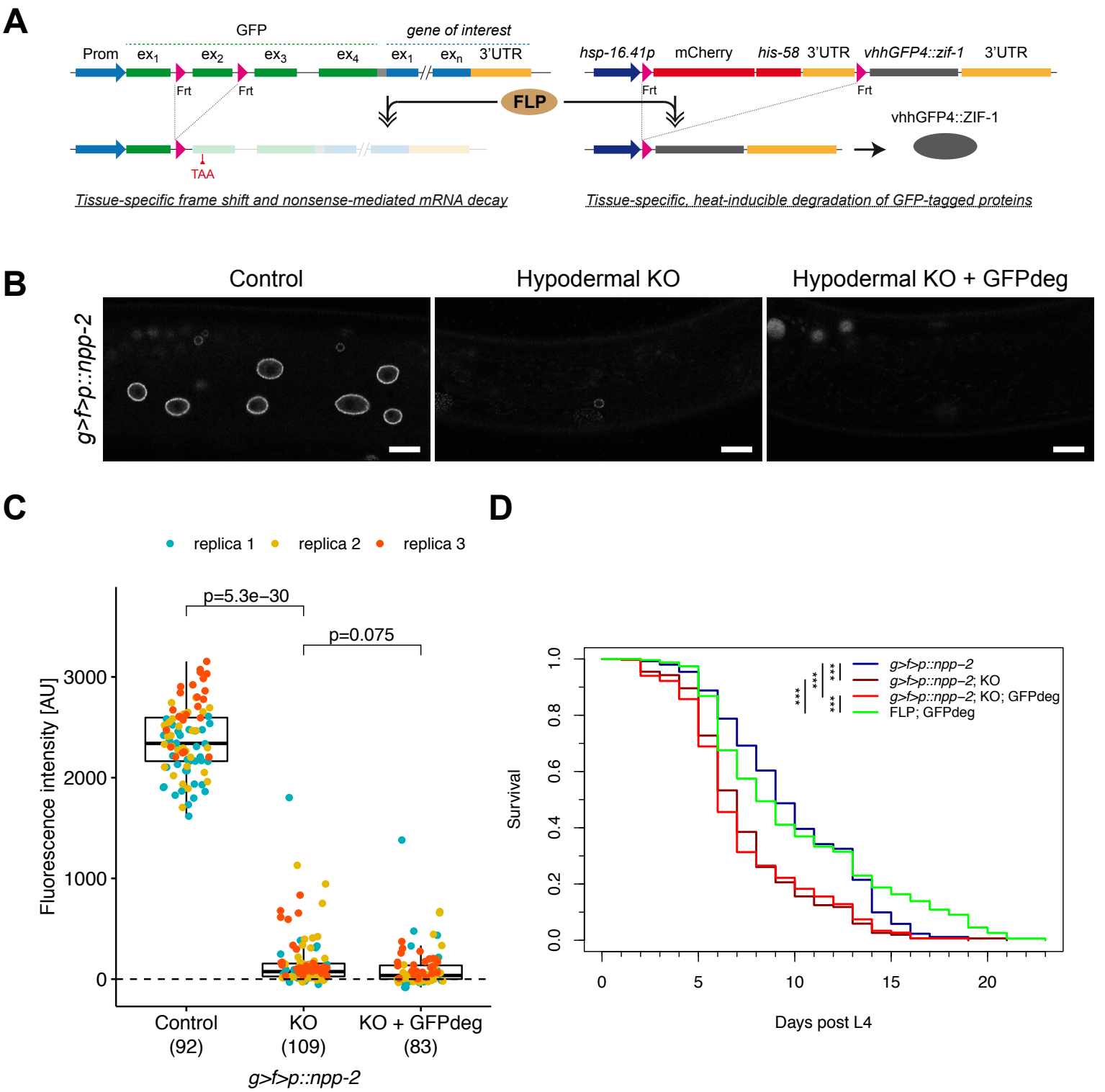
A
GFP
gene of interest
Prom
ex1
ex2
ex3
ex4
ex1
exn
3'UTR
Frt
Frt
FLP
TAA
hsp-16.41p
mCherry
his-58
3'UTR
vhhGFP4::zif-1
3'UTR
Frt
Frt
vhhGFP4::ZIF-1
Tissue-specific frame shift and nonsense-mediated mRNA decay
Tissue-specific, heat-inducible degradation of GFP-tagged proteins
B
Control
Hypodermal KO
Hypodermal KO + GFPdeg
g>f>p::npp-2
C
replica 1
replica 2
replica 3
p=5.3e−30
p=0.075
Fluorescence intensity [AU]
3000
2000
1000
0
Control
(92)
KO
(109)
KO + GFPdeg
(83)
g>f>p::npp-2
D
Survival
1.0
0.8
0.6
0.4
0.2
0.0
g>f>p::npp−2
g>f>p::npp−2; KO
g>f>p::npp−2; KO; GFPdeg
FLP; GFPdeg
***
***
***
***
0
5
10
15
20
Days post L4

Figure 7

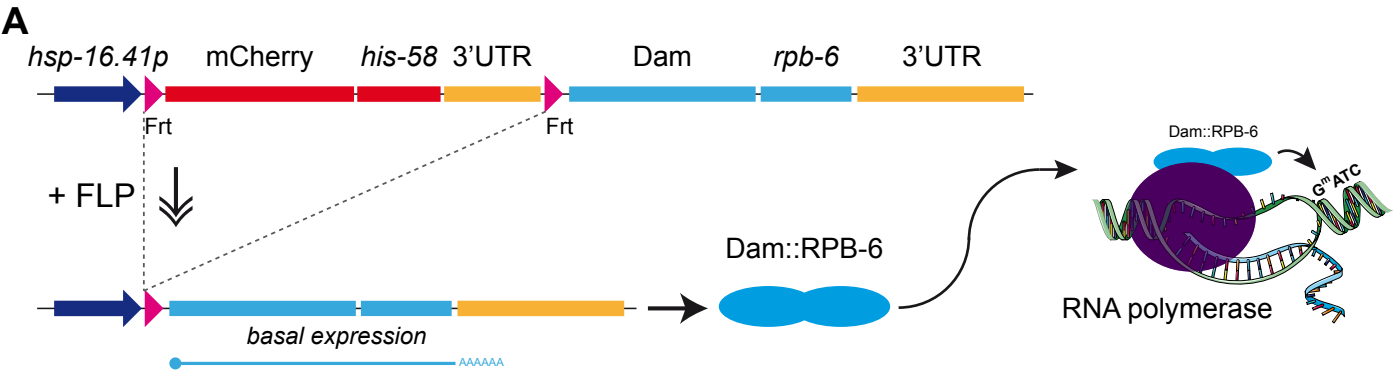

Tissue-specific labeling of transcribed genes (RNA polymerase DamID = RAPID)

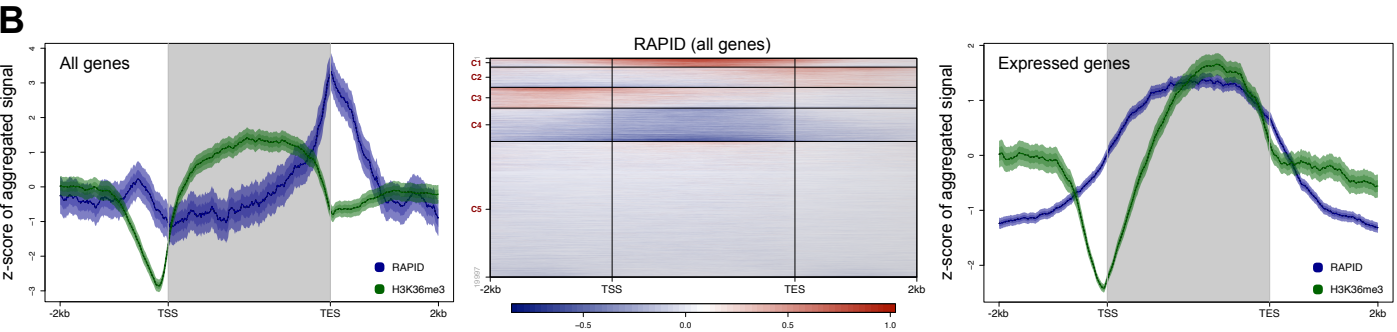

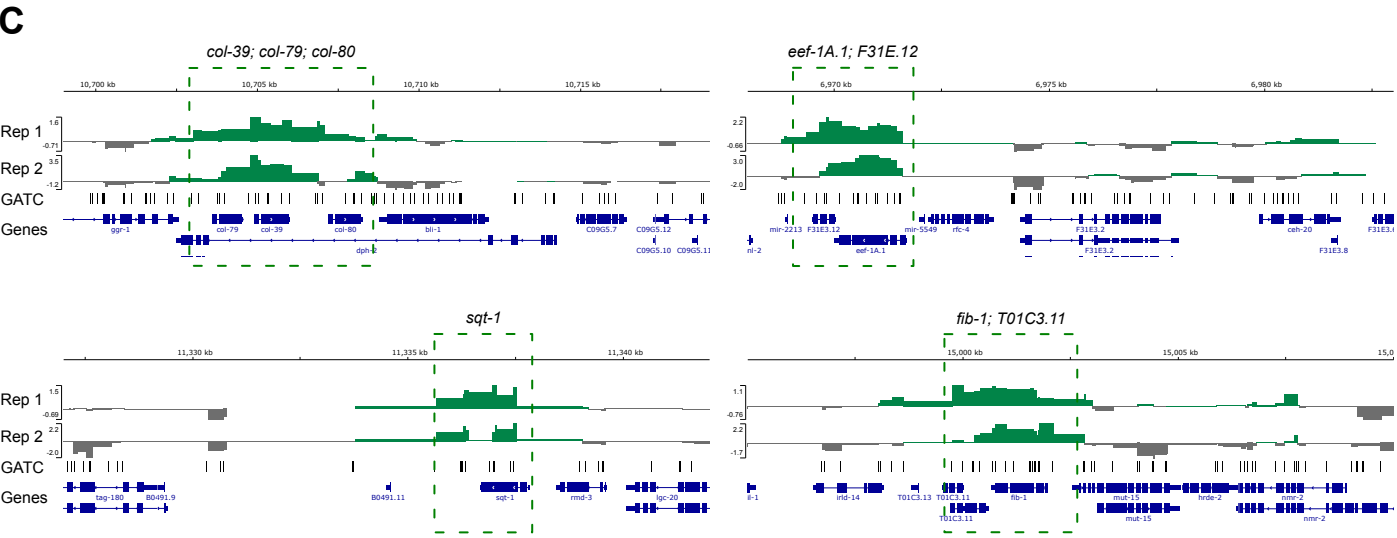

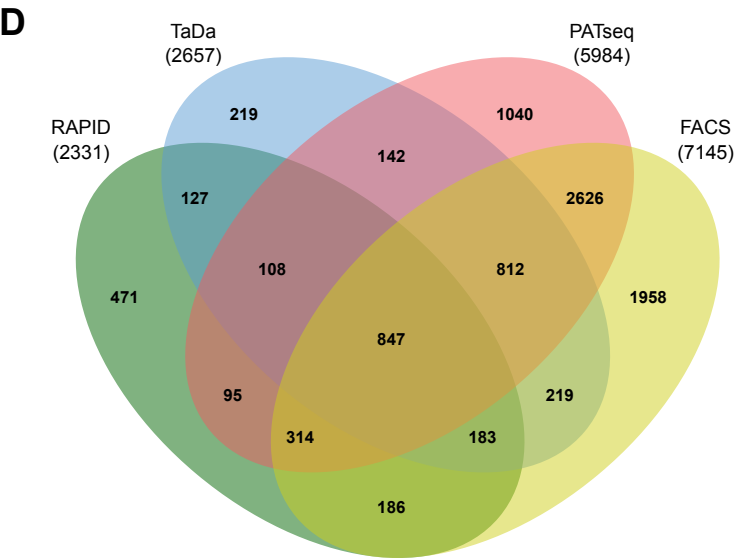

E

Fraction of \ In common with	RAPID	TaDa	FACS	PATseq
RAPID genes		54%***	66%***	59%***
TaDa genes	48%***		78%***	72%***
FACS genes	21%***	29%***		64%***
PATseq genes	23%***	32%***	77%***	